Measurement Criteria for the Magnetic Characterization of Magnetic Materials

Abdellahi Abderahmane, Laurent Daniel

TIM-23-04058

Measurement criteria for the magnetic characterization of magnetic materials

Abdellahi Abderahmane, Laurent Daniel., *Member, IEEE*

***Abstract*—Ferromagnetic materials exhibit nonlinear magnetic behavior, and many are anisotropic. Their magnetic characterization requires a mapping – in excitation and measurement – of the magnitude and direction of the magnetic field *H* or magnetic induction *B*. While many works from the literature have treated different parts of the characterization problem, the question of measurement reliability was not always adequately addressed. The present work relies on key assumptions made in characterization experiments to derive three criteria that form a necessary and sufficient condition for reliable measurements: (1) material properties are assumed homogeneous in the measurement region (uniformity criterion), (2) measured *H* is assumed to be equal to that giving rise to the measured *B*(correspondence criterion) and (3) *B&H* directions are assumed known (direction criterion). The fulfillment of these assumptions is assessed quantitatively based on various apparatuses found in the literature and new ones. Both alternating and rotating field loadings are considered for linear and nonlinear behaviors, using isotropic and anisotropic materials in both 1D and 2D excitation and measurement systems, with and without applied mechanical stress. The derived criteria provide guidelines for accepting, rejecting, and improving experimental apparatuses and offer clear insight into the measured data. In general, and when the application allows it, surface measurements of both *B&H* are recommended. 1D excitation systems – though limited to certain applications – fulfill the criteria the most.**

***Index Terms*—Magnetic measurement, Experimental characterization, Magneto-mechanical loadings, Sample design.**

I. INTRODUCTION

Ferromagnetic materials are used in various industrial applications. Understanding their behavior under different types of loadings (mechanical, electrical, magnetic, thermal) helps improve the design and extend the lifespan of electromagnetic devices. The present work deals mainly with the problem of magnetic characterization under applied magneto-mechanical loading. Such a problem has been treated both theoretically and experimentally by many authors in the literature ([1],[2],[3],[4],[5],[6],[7] to cite a few). However, to our knowledge, no works have provided rigorous studies on the requirements for an experimental apparatus to yield reliable behavior identification. A characterization apparatus can generally be divided into the sample, the excitation, and the measurement systems. Characterization is carried out under the hypothesis that the sample's magnetic properties are homogenous in the measurement region. In the case of a nonlinear behavior and an arbitrary anisotropy, the magnetic field $\boldsymbol{H}$ (or the magnetic induction $\boldsymbol{B}$) must be applied and measured in a 3D space. Two ways to do this are (a) fixing the field magnitude and varying its direction (the rotating loading) or (b) fixing the direction and varying the magnitude (the alternating loading). Note, however, that an apparatus equipped with 3D excitation and measurement parts and allowing the application of various loadings (e.g., mechanical or thermal) is challenging to design in practice. As a result, 1D and 2D excitation and measurement systems are often used. To compensate for the lost dimension(s), samples from the material are cut out at various orientations with respect to a characterization reference frame (denoted R_c). A reference frame R_s, attached to each sample (see Fig.1), is needed to map the results back to R_c. All works found in the literature adopted such a procedure. A non-exhaustive list of such works is given hereafter.

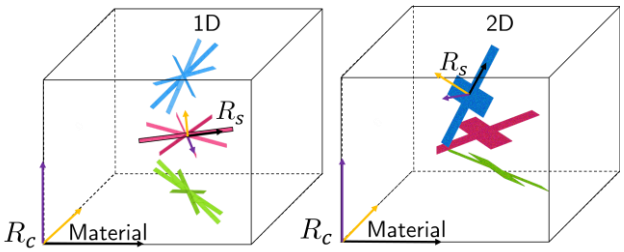

Fig.1. An illustration of samples cut at various orientations with respect to the characterization reference frame R_c. On the left (resp right), samples are used in 1D (resp 2D) excitation and measurement systems. To each sample is attached a reference frame R_s.

Sievert [8] treats the induction and measurement of both alternating and rotating magnetic fields. Five configurations are studied. In three of them, two ferromagnetic yokes are placed on either side of the sample (a steel sheet) to channel the

(Corresponding author: Abdellahi Abderahmane).

Abdellahi Abderahmane and Laurent Daniel are with the Laboratoire de Génie Électrique et Électronique de Paris, CentraleSupélec, Centre National de la Recherche Scientifique (CNRS), Université Paris-Saclay, 91192 Gif-sur-Yvette, France, and also with the Laboratoire de Génie Électrique et Électronique de Paris, Centre National de la Recherche Scientifique (CNRS), Sorbonne Université, 75252 Paris, France. (e-mail: abdellahi.abderahmane@centralesupelec.fr and laurent.daniel@centralesupelec.fr).

magnetic flux. The excitation coil is wound around the sample. In the first, one B-coil (wound around the sample section) and one H-coil (on one side of the sample) are used to measure $\boldsymbol{B}$&$\boldsymbol{H}$. In the second, $\boldsymbol{H}$ is measured using the magnetic path length, and in the third, a Rogowski-Coil. The fourth configuration has one yoke but two H-coils to compensate for the loss of symmetry (see Nakata *et al.* [9] for details). The fifth configuration uses a square sample placed between four yokes with an excitation coil wound around each yoke. Here an H-coil is used, and two sets of B-needles are used to measure $\boldsymbol{B}$ (details on the H-coil and the apparatus can be found in Enokizono *et al.* [10]). Zurek *et al.* [11] treated the problem of magnetic losses for conventional oriented and non-oriented electrical steels under a rotating magnetic field. The apparatus used a disc sample placed in a round magnetizing yoke. The sample was magnetized using two orthogonal coils. To measure $\boldsymbol{B}$, two orthogonal B-coils were wound through small holes drilled in the sample. The same apparatus was used in another experiment (Zurek *et al.* [12]), wherein the goal was to compare the power losses under controlled $\boldsymbol{H}$ and controlled $\boldsymbol{B}$. Here a 2 mm air gap was left between the yoke and the sample. Holes for the B-coils were drilled 20 mm apart, and the H-coil (in contact with the sample surface) was 20 mm wide. Stranges *et al.* [13] studied the possibility of predicting rotational power losses from alternating ones in non-grain-oriented and grain-oriented steels. The apparatus used in this experiment is similar to the fifth configuration in Sievert [8] and that of Brix *et al*. [14]. Here, however, holes were drilled in the sample to wind B-coils. Ramos *et al*. [15] used a similar apparatus to that of Stranges *et al.* [13], with the difference of using a cross-shaped sample. The particularity of Ramos *et al.* [15] work resides in measuring $\boldsymbol{B}$ by winding around the sample legs while measuring $\boldsymbol{H}$ (with an H-coil) at the sample center. Mori *et al.* [16] used finite element simulation to design an apparatus where various slits are made in the yokes to improve the field's uniformity. The sample consisted of a square-shaped steel sheet placed between two pairs of yokes. The excitation coils (orthogonal to each other) are wound around the sample. B-needles and H-coils were used to measure $\boldsymbol{B}$&$\boldsymbol{H}$. Ivanyi *et al.* [17] studied the case of a hexagonal-shaped sample. Six magnetizing yokes were used, and an air gap was left between the sample and the yokes. The types of sensors used for $\boldsymbol{B}$&$\boldsymbol{H}$ measurements were not disclosed. The works presented herein give a broad overview of the types of apparatuses used for stress-free magnetic characterization. Other works ([18],[19],[20],[21]) have treated the same problem; however, the apparatuses used are similar to the ones previously referred to. An apparatus capable of 3D excitation and measurement was treated in [22].

Thus far, the sample was subjected to only magnetic loading. The problem where both magnetic and mechanical loadings are considered adds to the complexity due to the strong magneto-mechanical coupling in ferromagnetic materials [1],[2]. Such a problem can be split into two categories: (a) uniaxial (the applied uniaxial stress is in the direction of the applied magnetic field) and (b) multiaxial (multiaxial stress is applied or the uniaxial stress is not in the direction of the applied magnetic field). The uniaxial problem does not generally suffer from stress non-uniformity and was the subject of numerous works [23],[24],[25],[26],[27],[28],[29],[30],[31],[32],[33],[34],[35]. The sample shapes can be parallelepipedal [25-29] or cylindrical [30]. $\boldsymbol{B}$ is measured using a B-coil wound around the sample cross-section, and $\boldsymbol{H}$, using an H-coil [28], a Hall sensor [25] or a magnetic incremental permeability sensor [32]. The excitation coil can be wound around the sample [23] or the yokes [25]. Both isotropic [24] and anisotropic [23] materials were studied in the elastic [29] and plastic [29],[31],[32] regimes for low [26] and high [30] frequencies. In contrast, far fewer works treat the multiaxial problem, and they deal mainly with in-plane biaxial loading. Nevertheless, some works [36],[37],[38] can be found where the magnetic field is applied in a direction different from that of the applied uniaxial stress. In [36], only a single C-yoke – that can be rotated – was used. The residual magnetic induction was measured as a function of applied stress using a tunneling magnetoresistance (TMR) sensor. In [37], compressive stress was normal to the sample surface while $\boldsymbol{B}$&$\boldsymbol{H}$ were in the plane. An H-coil was used to measure $\boldsymbol{H}$, and a flux density sensor was used to measure $\boldsymbol{B}$. Like the uniaxial case, this kind of multiaxial magneto-mechanical problem does not generally suffer from significant stress non-uniformity if these aspects are adequately addressed during the design of the sample. A study on stress uniformity in cross-shaped samples of various geometries subjected to uniaxial and biaxial loadings can be found in [39]. Langman [40] studied the effect of uniaxial and equibiaxial loadings on magnetic properties using a cross-shaped sample and a single C-yoke. The stress is introduced through bending. Sablik [41] treated a similar problem wherein the excitation coils were wound around the legs of a C-yoke placed on top of the sample. $\boldsymbol{H}$ was measured using a Hall sensor placed between the legs, and $\boldsymbol{B}$ using a search coil wound around one leg of the C-yoke. Similarly, to previous work, Rekik *et al*. [42] used a cross-shaped sample and a single C-yoke. However, here $\boldsymbol{H}$ was measured using an H-coil and $\boldsymbol{B}$, using B-needles. A cross-shaped sample with slits in its arms – to have a more uniform stress distribution – was also used by Kai *et al*. [43]. Excitation coils were wound around the sample arms, B and H-coils were used for $\boldsymbol{B}$&$\boldsymbol{H}$ measurements. A six-arm sample was used by Aydin *et al*. [44]. Such a sample allows the application of stress in an arbitrary in-plane direction. Excitation coils were wound around six separate yokes – forming the sides of a hexagon, whose diagonals are the sample's arms. $\boldsymbol{H}$ was measured using an H-coil, and $\boldsymbol{B}$ using B-coils positioned through drilled holes. Finally, Kai *et al*. [45] used an eight-arm sample with slits in the arms to study the effect of shear stress on magnetic properties. The excitation coils were wound around two yokes, and $\boldsymbol{B}$&$\boldsymbol{H}$ were measured using a vector-hysteresis sensor. These findings are summarized in Table I.

Though there is no shortage of experimental data in the literature, there seems to be no rigorous study assessing the reliability of experimental apparatuses. Such a study is the subject of the present work. A set of criteria that allows for accepting, rejecting, improving an experimental apparatus, and providing clear insight into the measurements is provided. These criteria are derived from the underlying assumptions made in every magnetic characterization experiment: (1) the material magnetic properties are homogeneous in the measurement region (uniformity criterion). (2) the measured magnetic field $\boldsymbol{H}$ is equal to the one giving rise to the measured

magnetic induction $\boldsymbol{B}$ (correspondence criterion). (3) $\boldsymbol{B}$&$\boldsymbol{H}$ directions are known throughout the experiment time (direction criterion). These criteria also apply to stress and strain and become even more urgent to meet for the magneto-mechanical problem due to the strong coupling. Such criteria are shown to form a necessary and sufficient condition for reliable measurements.

TABLE I

SUMMARY OF SOME EXPERIMENTAL APPARATUSES FROM THE LITERATURE USED FOR THE MAGNETIC CHARACTERIZATION OF MAGNETIC MATERIALS. THE FIRST COLUMN(S) GIVES THE TYPE OF PROBLEM TREATED (STRESS-FREE, UNDER UNIAXIAL OR BIAXIAL MECHANICAL STRESS). THE SECOND COLUMN GIVES THE CORRESPONDING REFERENCE NUMBER. THE THIRD, THE SAMPLE SHAPE, THE FOURTH, THE EXCITATION COIL (WOUND AROUND THE YOKE(S) OR THE SAMPLE). THE FIFTH AND THE SIXTH GIVE $\boldsymbol{B}$&$\boldsymbol{H}$ SENSORS. ABBREVIATIONS OF THE SAMPLE, EXCITATION COIL (EC), $\boldsymbol{B}$&$\boldsymbol{H}$ SENSORS ARE GIVEN IN THE LAST ROWS.

Problem			Ref	Sample								EC		B			H			
				Ss	Rs	Disc	Rod	Sp	Cs	6A	8A	Y	S	BN	BC	TMR	HS	HC	RC	MPL
Magnetic			8	•	•							•	•	•	•			•	•	•
			9		•								•		•			•		
			10		•							•			•			•		
			11			•						•			•			•		
			12			•						•			•			•		
			13	•								•			•			•		
			14					•				•			•			•		
			15					•				•			•			•		
			16	•									•	•				•		
			18		•							•			•		•			
			19			•						•			•			•		
			20		•		•					•		•			GMR			
			21		•								•	•				•		
			22	Cubic								•			•			•		
Magneto-Mechanical	Uniaxial	$(\boldsymbol{\sigma} \parallel \boldsymbol{H})$	23				•	•				•	•		•			•		
			25				•	•				•			•		•			
			26					•				•			•		•			
			27					•				•			•		•			
			28					•				•			•			•		
			29					•				•			•		•			
			30				•					•			•		•			
			31				•						•		•		•			
			32		•								•		•					•
			33		•							•			•		•	μ_{inc} sensor		
			34		•							•			•			•		
			35		•							•			•			•		
	Multiaxial	$(\boldsymbol{\sigma} \nparallel \boldsymbol{H})$	36					•				•				•				•
			37					•				•			•			•		
		Biaxial	40						•			•			•		•			
			41						•			•		•			•			
			42						•			•		•				•		
			43						•				•		•			•		
			44							•		•			•			•		
			45								•		•		•			•		

Abbreviation																				
Ss: square sheet			Rs: Rectangular sheet			Sp: Slender parallelepiped			Cs: Cross shape			6A: six arms			EC: excitation coil					
Y: Yoke		S: Sample		BN: B-Needle		BC: B-Coil		HS: Hall Sensor		HC: H-Coil		RC: Rogowski-Coil			MPL: Magnetic Path Length					

Simulation tools – which offer the necessary versatility and speed to study various apparatuses – are then used to assess the fulfillment of the criteria.

The present document is divided as follows: **Sec.II** provides mathematical proof of the measurement criteria's necessity and sufficiency. **Sec. III** deals with the fulfillment of the criteria. Various cases are studied: 1D (resp 2D) excitation systems are treated in **Sec.III-A** (resp **Sec.III-B**) for both isotropic and anisotropic materials, with and without applied mechanical stress under alternating and rotating magnetic fields. **Sec.IV** is the conclusion. Throughout the present document, bold notation is used for vectors and tensors.

II. THEORY

The present section demonstrates the necessity and sufficiency of the three criteria defined in the introduction. In the present work, the homogeneity assumption (*i.e.*, with no loading, magnetic properties are assumed homogeneous within the measurement region) is maintained. All three criteria are independent of time and thus apply to both anhysteretic and hysteretic behaviors.

A. Uniformity Criterion (UC)

To single out the question of uniformity, $\boldsymbol{B}$&$\boldsymbol{H}$ measurements regions are assumed to coincide, and their directions (at any point) are known. $\boldsymbol{B}$&$\boldsymbol{H}$ sensors have finite volumes; ergo, their output is an average over a given region. The uniformity criterion (*i.e.*, the homogeneity hypothesis should be respected) assesses whether the averaging operation yields the material behavior. Without loss of generality, the magnetic behavior can be described by the following equation:

$$\boldsymbol{B} = \boldsymbol{f}(\boldsymbol{H}) = \boldsymbol{\mu}(\boldsymbol{H}) \cdot \boldsymbol{H}. \tag{1}$$

$\boldsymbol{\mu}$ is the magnetic permeability; it can be a tensor or a scalar. The permeability also depends on other factors, such as the crystallographic structure and applied or residual stress. Call V the measurement region volume, the measured $\boldsymbol{B}$&$\boldsymbol{H}$ in this volume (denoted $\boldsymbol{H}^m$&$\boldsymbol{B}^m$) are given as follows:

$$\boldsymbol{H}^m = \frac{1}{V}\int_V \boldsymbol{H}(\boldsymbol{X})dV\,, \qquad \boldsymbol{B}^m = \frac{1}{V}\int_V \boldsymbol{B}(\boldsymbol{X})dV. \tag{2}$$

For each spatial point $\boldsymbol{X}$ in V, the relationship $\boldsymbol{B}(\boldsymbol{X}) = \boldsymbol{f}\big(\boldsymbol{H}(X)\big)$ is verified. Since $\boldsymbol{\mu}$ (representing the magnetic properties) depends on $\boldsymbol{H}$ which in turn depends on the position $\boldsymbol{X}$, the validity of the homogeneity hypothesis (which would imply $\boldsymbol{B}^m = \boldsymbol{f}(\boldsymbol{H}^m)$) in V is not always guaranteed. To assess such validity, V is discretized into N small elementary volumes v_n. The size of v_n is chosen so that $\boldsymbol{B}$, $\boldsymbol{H}$ and $\boldsymbol{\mu}$ are – practically – uniform and are denoted $\boldsymbol{B}_n, \boldsymbol{H}_n$ and $\boldsymbol{\mu}_n$. Eq (2) writes:

$$\boldsymbol{H}^m = \frac{1}{V}\sum_{n=1}^{N} v_n \boldsymbol{H}_n\,, \qquad \boldsymbol{B}^m = \frac{1}{V}\sum_{n=1}^{N} v_n \boldsymbol{B}_n, \tag{3}$$

Since in v_n the quantities $\boldsymbol{B}_n, \boldsymbol{H}_n$ and $\boldsymbol{\mu}_n$ are uniform (*i.e.*, independent of the position $\boldsymbol{X}$), the relationship $\boldsymbol{B}_n = \boldsymbol{f}(\boldsymbol{H}_n) = \boldsymbol{\mu}_n \cdot \boldsymbol{H}_n$ is also verified. Substituting $\boldsymbol{B}_n$ in Eq (3) yields:

$$\boldsymbol{B}^m = \frac{1}{V}\sum_{i=1}^{n} v_n \boldsymbol{f}(\boldsymbol{H}_n). \tag{4}$$

The following relationship

$$\boldsymbol{f}(\boldsymbol{H}^m) = \boldsymbol{f}\left(\frac{1}{V}\sum_{n=1}^{N} v_n \boldsymbol{H}_n\right) = \frac{1}{V}\sum_{n=1}^{N} v_n \boldsymbol{f}(\boldsymbol{H}_n) = \boldsymbol{B}^m, \tag{5}$$

is true *if and only if* the function $\boldsymbol{f}$ is linear for all $\boldsymbol{H}(\boldsymbol{X})$ where $\boldsymbol{X} \in V$. Note that since $\boldsymbol{H}$ is a vector, $\boldsymbol{f}$ needs to be linear for both the field magnitude and direction. As a result, non-uniformity – in field direction and magnitude – does not affect isotropic materials exhibiting linear behavior. For isotropic materials with nonlinear behavior, its effect is minimal around saturation (where the behavior is relatively linear) and maximal around the knee of the $B(H)$ curve (norm of $\boldsymbol{B}$ as a function of the norm of $\boldsymbol{H}$). The effect on anisotropic linear or nonlinear materials depends on the type of anisotropy. In conclusion, *high non-uniformity does not always equate to high error*. For convenience, non-uniformity in the measurement region can be split into 1) through-thickness and 2) in-plane. To minimize the effect of the first, the excitation frequency can be decreased to reduce the effect of eddy currents until measurements are no longer dependent on it. For the second, the region on which the measurements are averaged can be reduced (it needs, however, to be large enough to be representative of the material).

B. Direction Criterion (DC)

To single out the question of direction, $\boldsymbol{B}$&$\boldsymbol{H}$ measurements regions are assumed to coincide, and their distributions (magnitude and direction) are uniform. $\boldsymbol{B}$&$\boldsymbol{H}$ sensors measure the projections of fields in 1, 2, or 3 directions. Since the field's direction and magnitude cannot, in general, be deduced from 1 or 2 projections, the direction criterion ($\boldsymbol{B}$&$\boldsymbol{H}$ directions should be known) becomes mandatory. To prove this, call (θ_B, ϕ_B) and (θ_H, ϕ_H) the angles defining $\boldsymbol{B}$&$\boldsymbol{H}$ directions in R_s (the sample reference frame). Consider the case where only single-axis (one projection) sensors are used to measure $\boldsymbol{B}$&$\boldsymbol{H}$. Without loss of generality, these sensors are assumed to measure the components in the x-direction (*i.e.* B_x&H_x). Consequently, the $B = f(H)$ curve is now replaced by the curve $B_x = f(H_x)$. Since $B_x = \sin(\theta_B)\cos(\phi_B)\,B = k_B B$ and $H_x = \sin(\theta_H)\cos(\phi_H)\,H = k_H H$, the equation $B_x = f(H_x)$ is now rewritten as:

$$B = \frac{1}{k_B} f(k_H H) \tag{6}$$

In the case where $\boldsymbol{B} \parallel \boldsymbol{H}$ one has $k_B = k_H$ as a result, the $B_x = f(H_x)$ curve is the image of the $B = f(H)$ curve under a

pseudo-homothety of coefficient k_B. Such transformation is not a real homothety since $k_B = \sin(\theta_B)\cos(\phi_B)$, depends on the direction of $\boldsymbol{B}$. If, on the other hand $\boldsymbol{B} \nparallel \boldsymbol{H}$, the $B_x = f(H_x)$ is a distorted image of that of $B = f(H)$ (*i.e.*, shrinking the H-axis with k_H and the B-axis with k_B). This result is generalized to the 2D case where double-axis sensors (two projections) are used (here, $k_B = \sin(\theta_B)$ and $k_H = \sin(\theta_H)$). In conclusion, *the field directions should be known*; otherwise, the 1D and 2D measurements can yield distorted images of the real behavior. Such directions can be known in practice by measuring in three orthogonal directions (the out-of-plane $\boldsymbol{B}$ component can be measured using the continuity of the normal magnetic induction component boundary condition).

C. Correspondence Criterion (CC)

To single out the question of correspondence, $\boldsymbol{B}$&$\boldsymbol{H}$ distributions (magnitude and direction) are uniform, and their directions are known. The correspondence criterion stipulates that the measured $\boldsymbol{H}$ should correspond (be equal) to the one giving rise to the measured $\boldsymbol{B}$. Such a criterion is necessary for two reasons: (1) the measurement regions of $\boldsymbol{B}$&$\boldsymbol{H}$ are generally distinct ($\boldsymbol{B}$ is measured within the material volume while $\boldsymbol{H}$ outside the material volume); (2) since $\boldsymbol{B}$&$\boldsymbol{H}$ are vectors, the orientations of their corresponding sensors are needed to define them uniquely. The consequence of (1) is that the measured magnetic field (call it $\boldsymbol{H}^m$) is generally different (in magnitude and direction) from the magnetic field (call it $\boldsymbol{H}$), giving rise to the measured $\boldsymbol{B}^m$. The relationship between the two can be written as follows: $\boldsymbol{H}^m = \boldsymbol{A}(\boldsymbol{\mu}) \cdot \boldsymbol{H}$, where $\boldsymbol{A}$ is a 2x2 tensor that depends on the experimental apparatus and the material properties. As a result, not respecting the correspondence criterion compromises the reliability of all measurements – except the ones involving only $\boldsymbol{B}$. In practice, to overcome such an issue, $\boldsymbol{B}$&$\boldsymbol{H}$ measurement regions should coincide or at least be as close to each other as possible. Such a condition is met when $\boldsymbol{H}$ measurement is carried out at the sample surface (assuming a through-thickness uniformity). It is worth emphasizing that when both $\boldsymbol{B}$&$\boldsymbol{H}$ are measured at the surface, through-thickness uniformity is not mandatory. As a result, measurements can be carried out at relatively higher frequencies.

To study the effect of misorientation (2), $\boldsymbol{B}$&$\boldsymbol{H}$ measurement regions are chosen – without loss of generality – to coincide. Two cases can be distinguished:

(a) no misorientation is present between $\boldsymbol{B}$&$\boldsymbol{H}$ sensors; however, there is one between the sensors and the sample reference frame R_s. In this case, isotropic materials are unaffected since to such materials R_s orientation – with respect to the characterization reference frame R_c – is of no importance. As for anisotropic materials, this translates to the measured material properties to be the image of the real ones under the rotation $rot(R_s \rightarrow R_B)$, where R_B is the reference frame attached to the $\boldsymbol{B}$ sensor.

(b) R_s, R_B and R_H (the reference frame attached to the $\boldsymbol{H}$ sensor) all have different orientations with respect to R_c. Let $\boldsymbol{C}_{BH}$ be the direction cosines matrix between R_B and R_H (i.e., the product of the three rotation matricies around R_B axes). For isotropic materials the constitutive relation $B(H)$ becomes $\boldsymbol{B} = \mu(H)[\boldsymbol{C}_{BH} \cdot \boldsymbol{H}]$. The fact that the norm of $\boldsymbol{C}_{BH} \cdot \boldsymbol{H}$ is equal to H shows that measurements involving only the field norms are unaffected. Additionally, measurements involving only each of the fields alone (*e.g.*, $B_y(B_x), B_z(B_x), H_y(H_x), H_z(H_x)$ ...) are also unaffected. However, those mixing the fields (*e.g.*, $B_x(H_x)$, $B_y(H_y)$...) are affected since they depend on the components of $\boldsymbol{C}_{BH}$. Due to the presence of $\boldsymbol{C}_{BH}$ (i.e., a tensor) the fields $\boldsymbol{B}$&$\boldsymbol{H}$ are now non-colinear for isotropic materials. This observation shows that such materials can, in principle, be used in a calibration step to gauge misorientation between these sensors. As for anisotropic materials, only the measurements, including the fields' norms, remain unaffected.

The misorientation between sensors differs from the one given by (a) because material properties are not the images of the real ones under any rotation. This is because misorientation between R_B and R_H can render non-colinear fields colinear and vice-versa. In practice, isotropic materials can be used in a calibration step to reduce sensor misorientation.

In summary, the three criteria' fulfillment is necessary for reliable magnetic characterization. If not guaranteed, various errors that add to or subtract from each other can emerge. When all three criteria are combined, they form a sufficient condition. This is evident since their combination yields a known and unique load ($\boldsymbol{H}$) and material response ($\boldsymbol{B}$), which correspond to each other. The next section assesses the fulfillment of the criteria derived herein for various types of apparatuses using simulation. Though these criteria apply for hysteretic and anhysteretic behaviors, simulations were carried out under the latter.

III. SIMULATION

The fulfillment of the $\boldsymbol{B}$&$\boldsymbol{H}$ measurements criteria (BHmC) is assessed through various studies. Both alternating and rotating field loadings are considered for isotropic and anisotropic materials in 1D and 2D excitation systems, with and without applied stress. In all studies, currents are imposed. All apparatuses have one sample, yokes, and excitation coils (material properties given in Table II).

TABLE II
MATERIAL PROPERTIES

Properties	Yoke	Sample	Coil
ϵ[F/m]	ϵ_0	ϵ_0	ϵ_0
σ[S/m]	1	Case dependent	6e7
μ[H/m]	1e4/8e4	Case dependent	1

While studies were carried out for both linear and nonlinear behaviors, the results shown here correspond to the latter. However, conclusions from the linear cases are recalled if need be. Unless specified otherwise, the excitation frequency and samples' thickness (10 mHz, and 2 mm in all cases) are chosen to achieve through-thickness uniformity for all studied materials. In practice $\boldsymbol{B}$&$\boldsymbol{H}$ sensors output voltage signals from which the field magnitude and direction are inferred. To avoid errors due to sensor design and precision, points, surfaces, and volumes are used in the present section to model the sensor's effective area. For each study, one or more of the following six results are presented: (1) the real material behavior, (2) measurements at a single point (all three criteria are met), (3) at the sample surface (the uniformity criterion is not necessarily

met), (4) above the sample surface with no misorientation and with triple-axis sensor (only orientation criterion is met), (5) with $\boldsymbol{B}$&$\boldsymbol{H}$ sensors misorientation (only orientation criterion is met), and (6) with single-axis or double-axe sensors but without misorientation (all three criteria are not met). Further complementary results, and conclusions from studies not shown (due to lack of space) particular to each case, shall be provided for clarity. All simulations are carried out using COMSOL Multiphysics™. For each study, the mesh type (resp size) was systematically adapted (resp refined) to have accurate results (*i.e.*, independent of the mesh).

A. 1D systems

A typical apparatus used for 1D characterization is presented in Fig.2. Only one-quarter of the apparatus is shown (Fig.2(a)). Such apparatus can be used to characterize both isotropic and anisotropic materials. The BHmC are tested first for the isotropic case.

Each $\boldsymbol{H}$ field component is averaged over the corresponding $1 \times 2\text{mm}^2$ plate (which represents the effective area of a Hall sensor). R_H is centered at 1.5 mm from the sample surface. For this 1D system R_B coincides with R_s. The $\boldsymbol{B}$ measurement region is represented by a blue parallelepiped, over which the $\boldsymbol{B}$ field norm or B_z component are averaged (which emulates the effective area of a B-coil, wound around the sample section).

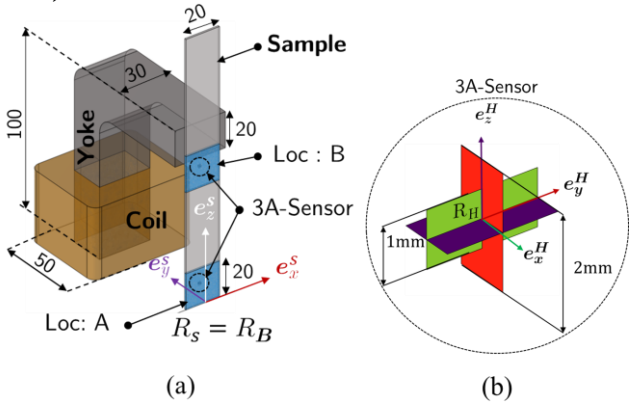

Fig.2. Typical apparatus used for 1D characterization (all dimensions are in mm). (a) one-quarter of the apparatus. (b) a zoom-in on the triple-axis sensor (3A-Sensor) used for $\boldsymbol{H}$ field measurement. R_H is the reference frame attached to the 3A-Sensor and is centered at 1.5 mm above the surface.

1. Isotropic materials

For the present case, characterization is carried out at two locations. The first (denoted Loc: A) is close to the sample center, and the second (denoted Loc: B) is close to the yoke end (see Fig.2). In Fig.3(a) "BH" (dot marker) gives the real magnetic behavior of the sample material (i.e., the B(H) curve used to run the simulation). "Point" (solid black line) gives $B = f(H)$, at a single point (inside the sample) in the blue region. "Surface" ("x" marker) gives $avg(B) = f\big(avg(H)\big)$ at the sample surface. "3A" (green solid line) gives $avg(B) = f\big(avg(H)\big)$, where $\boldsymbol{B}$ is averaged over the blue volume, and $\boldsymbol{H}$ measured using the 3A-sensor (see Fig.2(b)). "1A-surface" (circular marker) gives $avg(B_z) = f\big(avg(H_z)\big)$ at the sample surface. "1A" (diamond marker) gives $avg(B_z) = f\big(avg(H_z)\big)$, where the average of H_z is measured using a single-axis sensor (*i.e.*, one plate of the 3A-sensor given in Fig.2(b)). Finally, "1A-Mis" (square marker) gives $avg(B_z) = f\big(avg(H_z')\big)$, where H_z' is given by $H_z' = (\boldsymbol{C_{H\to S}} \cdot \boldsymbol{H}) \cdot \boldsymbol{e_z^H}$ ($\boldsymbol{C_{H\to S}}$ is the direction cosines matrix between the sample reference and that of the $\boldsymbol{H}$ field sensor). In this example $\boldsymbol{C_{H\to S}}$ is the rotation matrix of 30 deg angle around the $\boldsymbol{e_y^S}$-axis. Other studies used smaller misalignments (2.5, 5, 10, 15, and 20 deg). Their deviations, however, were small, making them visually tricky to distinguish from the real material behavior, thus the choice of the larger 30 deg angle. At loc-A, all results, except the one with misorientation, practically coincide with the real material behavior. The reason for this is that at loc-A, both $\boldsymbol{B}$&$\boldsymbol{H}$ fields are practically in the $\boldsymbol{e_z^S}$-direction (i.e., along the sample length). This is shown in Fig.3(c), where the direction cosines ($100H_i/H$ and $100B_i/B$ denoted X where $i \in \{x, y, z\}$) are given as a function of the experiment time. The small nonnull H_y component at this location was shown – in a separate simulation – to depend on the distance between the sample and the 3A-sensor. Fig.3(b) gives the same results but at location B. Only the results corresponding to the single point measurement (taken at the center of the blue region at location B and where all BHmC are respected) coincide with the real material behavior. The coincidence between "Surface" and "1A-surface" shows that both fields at the surface are in the z-direction, which shows that the deviation from the real behavior is due to an ill-respected uniformity criterion (UC). At this location, the result with misorientation is closer to the real material behavior than that without it (square marker). The same is true for the result using a single-axis sensor (diamond marker) compared to that using a 3A-sensor (solid green line where the error can be 80%). This observation confirms that errors emerging from ill-respected BHmC can add to or subtract from each other. Fig.3(c) shows that at this location, the $\boldsymbol{H}$ field changes its direction throughout the experiment, which can only be detected when carrying out 3D measurements. To showcase the effect of the through-thickness non-uniformity – thus far guaranteed due to the low frequency (10mHz) – location A is chosen for the measurement at different frequencies. Besides the real material behavior (dot marker), Fig.3(d) gives measurements for 100 Hz and 500 Hz. In all three curves, the $\boldsymbol{B}$ field norm ($\approx B_z$) is measured in the material volume, the $\boldsymbol{H}$ field is measured at the surface (100Hz:H-S and 500Hz:H-S) and above the surface at the 3A-sensor position (500Hz:H-3A). Note how measurements strongly depend on the frequency. Since in-plane uniformity is guaranteed at location A (this was also verified here), the deviations of 100Hz:H-S and 500Hz:H-S from the real material behavior are solely due to through-thickness non-uniformity. The deviation of 500Hz:H-3A results from both an ill-respected uniformity and correspondence criteria. Note how close to saturation the curves at high frequencies coincide with $B(H)$. This is due to the low permeability around saturation, which yields a large skin-depth and, thus, a better through-thickness uniformity. Finally, the curve corresponding to measurements at the surface for both $\boldsymbol{B}$&$\boldsymbol{H}$ (not shown for clarity) was shown to coincide with real material behavior. The dependence of the fulfillment criteria on the sample material properties is shown in Fig.3(e-f) wherein a different material is used. Such dependence is evidenced by

how large the discrepancies at location-B are, compared to those of the first material (Fig.3(b)). Conclusions from complementary studies with different yoke permeabilities (1000 and 80000) and various sample materials are identical to the ones presented herein. In conclusion, location A is better for this apparatus and can be improved by moving the $\boldsymbol{H}$ sensor close to the sample surface and, if possible, carrying out both $\boldsymbol{B}$&$\boldsymbol{H}$ measurements at the surface. Furthermore, these results show that some configurations found in the literature [15] and [41] should be avoided: (a) measuring close to the yoke ends (b) having the $\boldsymbol{B}$&$\boldsymbol{H}$ measurement regions far apart. These two imply that measuring $\boldsymbol{H}$ using the magnetic path [32] and [36] length is inadequate since BHmC are hardly respected. And finally, measurements using a B-coil while there is through-thickness non-uniformity. Studies, wherein the 3A-Sensor was closer to the sample edges and others using sensors representing H-coils (instead of Hall sensors) were carried out; however, the conclusions remained the same as the ones presented herein. A complimentary simulation using linear behavior showed that measurements at the surface for both locations were the same, confirming that for linear isotropic materials the uniformity criterion is always met.

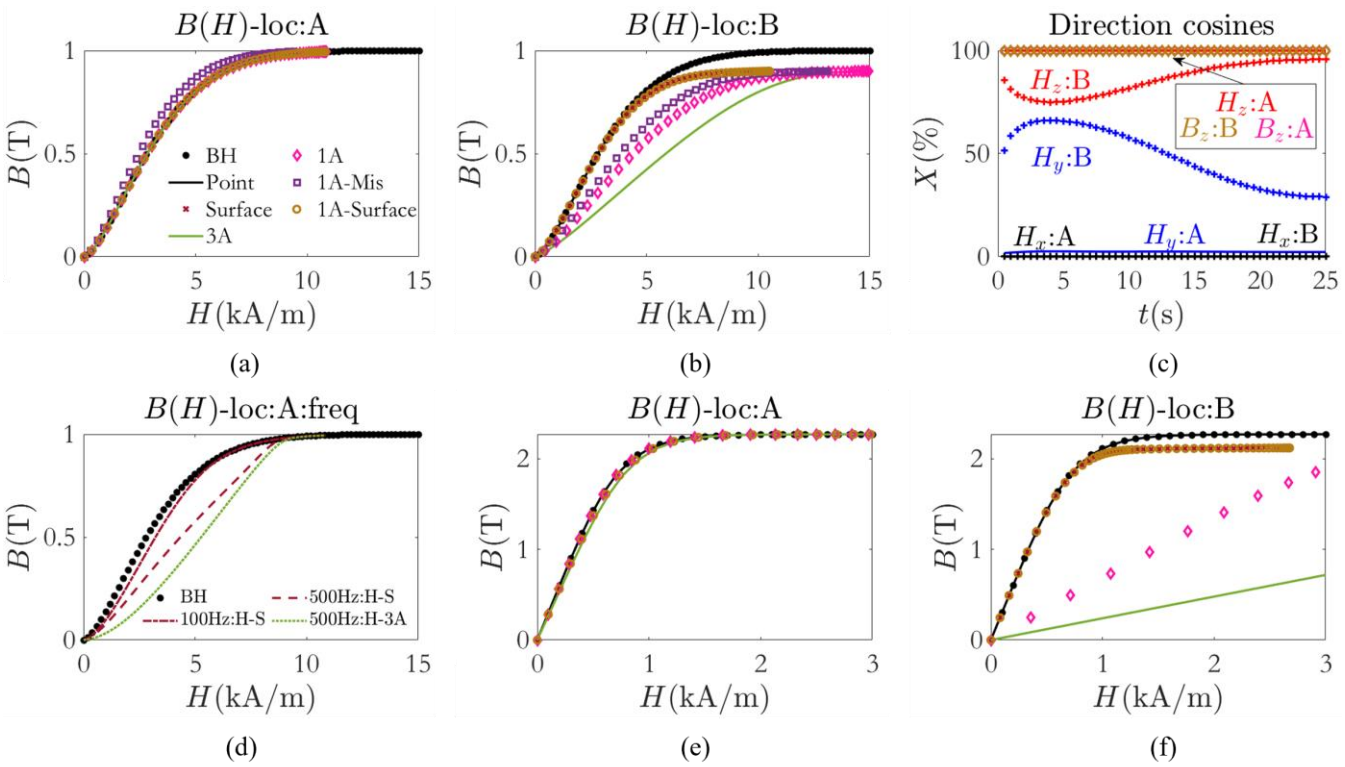

Fig.3. (a) (resp (b)) measurement carried out at location A (resp B). Dot marker: the real material behavior. Point: measurements (of both $\boldsymbol{B}$&$\boldsymbol{H}$) at a single point inside the sample. Surface: measurement (of both $\boldsymbol{B}$&$\boldsymbol{H}$) at the surface. 3A: $\boldsymbol{B}$ is measured in the sample and $\boldsymbol{H}$ above the sample using the 3A-sensor. 1A: like 3A, here, however, only a single-axis sensor is used for $\boldsymbol{H}$. 1A-Mis: measurements with 30 deg $\boldsymbol{B}$&$\boldsymbol{H}$ misalignment. 1A-surface: similar to 1A, however only B_z is used instead of the norm of $\boldsymbol{B}$. (c) gives the direction cosines of both vectors $\boldsymbol{B}$&$\boldsymbol{H}$ ($100H_i/H$ and $100B_i/B$) in the sample reference frame. In (c), $\boldsymbol{H}$ components at location A are given by solid lines and at B by "+" markers. (d) measurements at different frequencies (100 and 500 Hz): $\boldsymbol{B}$ is measured in the volume while $\boldsymbol{H}$ at the surface (H-S) and above the surface (H-3A). (e) and (f) the same as (a) and (b) but for a different material.

2. Anisotropic material

Throughout the present document, the permeability for anisotropic materials is chosen elliptic ($\boldsymbol{\mu} = diag(\mu_a, \mu_b, \mu_c)$). Fig.4 shows $\boldsymbol{\mu}$ for two values of $\boldsymbol{H}$ magnitude (H_1: light grey and H_2: dark grey ellipsoids). Note that for a linear behavior, there is only a single ellipsoid. The reference $R_\mu(\boldsymbol{e_x^\mu}, \boldsymbol{e_y^\mu}, \boldsymbol{e_z^\mu})$ is attached to $\boldsymbol{\mu}$-ellipsoid. For the sake of generality both $\boldsymbol{\mu}$-ellipsoid shape (given by μ_a, μ_b and μ_c) and orientation with respect to R_c, can depend on H and other factors (denoted $\boldsymbol{\Lambda}$) such as applied or residual stress. Euler angles between R_c and R_μ are denoted by φ_1, ψ and φ_2 (around $\boldsymbol{e_z^c}, \boldsymbol{e_y^c}$ and $\boldsymbol{e_x^c}$), and the direction cosines matrix (corresponding to the sequence $\boldsymbol{e_z^c} \rightarrow \boldsymbol{e_y^c} \rightarrow \boldsymbol{e_x^c}$) by $\boldsymbol{C}$.

Throughout the present document, the dependence of ϕ_1, ψ and ϕ_2 on $\boldsymbol{\Lambda}$ and H, is described as follows: $\phi_1(\boldsymbol{\Lambda}, H) = \phi_1(\boldsymbol{\Lambda}) + \phi_1(H)$ (identical decomposition is done for ψ and ϕ_2). In the present paragraph, R_μ is chosen to coincide with R_c (*i.e.*, $\phi_1(\boldsymbol{\Lambda}) = \phi_1(H) = \psi(\boldsymbol{\Lambda}) = \psi(H) = \phi_2(H) = \phi_2(\boldsymbol{\Lambda}) = 0$). Four samples (Sx, Sy, Sz and Sxz) are studied: the first cut along the $\boldsymbol{e_x^c}$ direction, the second $\boldsymbol{e_y^c}$, the third $\boldsymbol{e_z^c}$ and the fourth is cut in the $(\boldsymbol{e_x^c}, \boldsymbol{e_z^c})$ plan at 30 deg angle from $\boldsymbol{e_z^c}$.

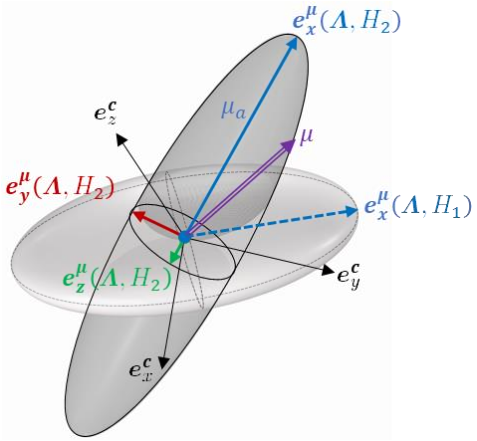

Fig.4. Elliptic permeability $\boldsymbol{\mu}$. Light grey (resp dark grey) ellipsoid corresponds to $H = H_1$ (resp $H = H_2$). $R_c(\boldsymbol{e}_x^c, \boldsymbol{e}_y^c, \boldsymbol{e}_z^c)$ (resp $R_\mu(\boldsymbol{e}_x^{\boldsymbol{\mu}}, \boldsymbol{e}_y^{\boldsymbol{\mu}}, \boldsymbol{e}_z^{\boldsymbol{\mu}})$) is the characterization (permeability) reference frame.

In this paragraph, the simulation is carried out a location A. It was found that, for the three samples cut along the principal permeability axes, $\boldsymbol{B}$&$\boldsymbol{H}$ are colinear, and their direction – practically constant – is along the sample(s) length ($\boldsymbol{e}_z^S$). As a result, all three principal permeability were obtained using $\mu_i = B_z^{Si}/\mu_0 H_z^{Si}$ where $i \in \{\mathrm{x}, \mathrm{y}, \mathrm{z}\}$. These permeabilities were calculated from measurements at a single point, on the surface, and above the surface (using 1A sensor for the $\boldsymbol{H}$); however, no significant discrepancies were found between them and the ones describing the real material behavior. As for the sample Sxy, the simulation showed $B_x \approx B_y \approx 0$, however, $\boldsymbol{B}$&$\boldsymbol{H}$ were not colinear, and the direction of $\boldsymbol{H}$ changed significantly throughout the experiment. On the one hand, using S_{xz}, can, in practice, be disadvantageous for characterization since 3D measurements are needed. On the other hand, such a sample offers a way to measure simultaneously both μ_a and μ_c. To illustrate this, Eq (1) is written in the sample reference frame as $\boldsymbol{B} = \left[\boldsymbol{C}_{\boldsymbol{\mu}\to\boldsymbol{Sxz}} \cdot \boldsymbol{\mu} \cdot \boldsymbol{C}^T_{\boldsymbol{\mu}\to\boldsymbol{Sxz}}\right] \cdot \boldsymbol{H}$, where $\boldsymbol{C}_{\boldsymbol{\mu}\to\boldsymbol{Sxz}}$ is the direction cosines matrix mapping R_μ to R_{Sxz}. In the present case R_{Sxz} is found by rotating R_μ around $\boldsymbol{e}_y^c$ by 30 deg angle. Upon doing the calculations, one finds:

$$\mu_a = \frac{\sqrt{3}B_x + B_z}{\mu_0\left(\sqrt{3}H_x + H_z\right)} \tag{7a}$$

$$\mu_c = \frac{\sqrt{3}B_x - B_z}{\mu_0\left(\sqrt{3}H_x - H_z\right)} \tag{7b}$$

Though it is possible to compute also μ_b, from the simulation results (since the out-of-plane components B_y and H_y are not exactly equal to zero in this example); in practice, small magnitudes are difficult to measure accurately. Fig.5(a) gives the three principal permeabilities computed from samples Sx, Sy and Sz (dot markers). Dashed (resp dotted) lines give μ_a&μ_c computed from the sample Sxz for measurement made at the surface (resp above the surface using 1A sensor for $\boldsymbol{H}$). The discrepancies between the two results stem from the fact that the fulfillment of BHmC varies from sample to sample. Here, for example, it is that of the correspondence criterion (CC) since the difference between the $\boldsymbol{H}$ field on the surface and above the surface is much larger for Sxz than the other samples (see Fig.5(b), which gives the direction cosines as functions of the experiment time).

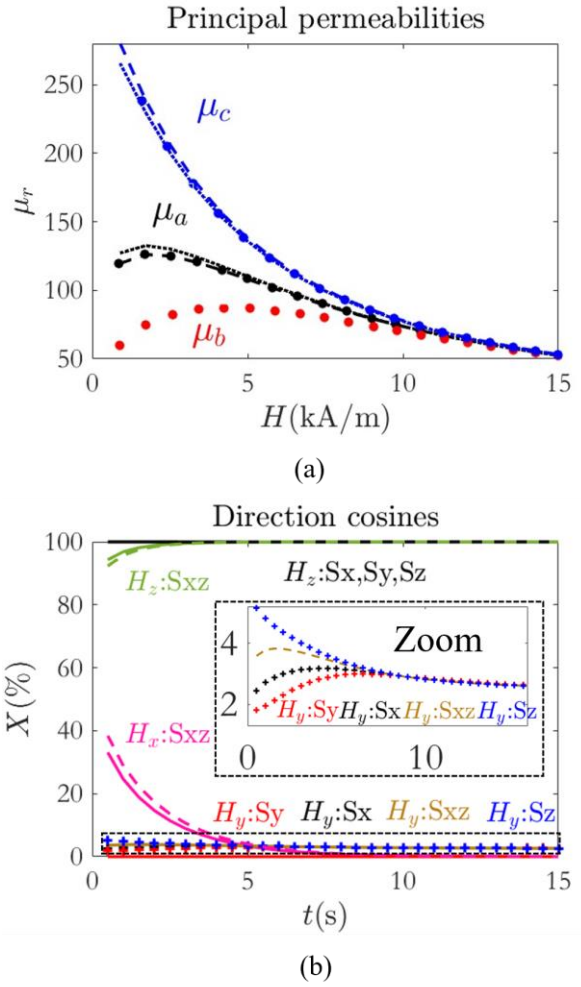

Fig.5. (a) dot makers give the principal permeabilities computed from measurements carried out using the samples Sx, Sy and Sz (*i.e.*, samples cut along the principal permeability axes). Dashed (resp dotted) lines give μ_a&μ_c computed from measurements carried out at the Sxz surface (resp above the surface). (b) Direction cosines of $\boldsymbol{H}$ for all samples: those of Sx, Sy and Sz at the surface (not shown for lack of space) are practically the same as the ones above the surface. Red (resp black) line corresponds to H_x: Sx, Sy, Sz (resp H_z: Sx, Sy, Sz). Solid green, pink, and brown (resp dashed) lines correspond to Sxz at the surface (resp above the surface).

Complementary cases were studied: in the first, the disparity between the principal permeabilities was more pronounced; in the second, the sample width was 80 mm (instead of 20 mm) and in the third, the $\boldsymbol{\mu}$-ellipsoid direction was dependent on the norm of the field. All cases showed that, in general, $\boldsymbol{B}$ is not always along the sample length. To overcome such an issue, in practice, the search coil wound around the sample should be replaced by a sensor that allows measuring at least two components (*e.g.*, B-needles). In conclusion, the present

paragraph showed that, in addition to the sample geometry and measurement location, the orientation of the cut sample also affects the fulfillment of the measurement criteria. In practice, for this particular apparatus, narrower samples are better, and in general, ***H*** should be measured as close to the surface as possible.

B. 2D systems

The characterization of a nonlinear anisotropic material (with unknown anisotropy) requires full mapping of both the field magnitude (from low to saturation) and direction (in 3D space). Though such mapping can be carried out randomly, applications from the literature follow two "ordered" approaches (loadings): fixing the direction and varying the magnitude (alternating) or fixing the magnitude and varying the direction (rotating). Only 2D excitation systems allow for the implementation of the second approach. The fulfillment of BHmC is studied for both isotropic and anisotropic materials. While characterizing anhysteretic isotropic materials does not require the use of a 2D system, such materials enable assessment of the "unwanted" change of direction (resp magnitude) in the alternating (resp rotating) approach. Aside from allowing for gauging the misorientation between ***B***&***H*** sensors, isotropic materials help also isolate and study the effect of nonlinearity in the rotating approach. In total, six different apparatuses are studied (see Fig.6). Three of which allow the application of only uniaxial stress, and the other three, the application of both uniaxial and biaxial stress. A 1 mm air gap is left between the yoke(s) and the sample for all apparatuses in the present document.

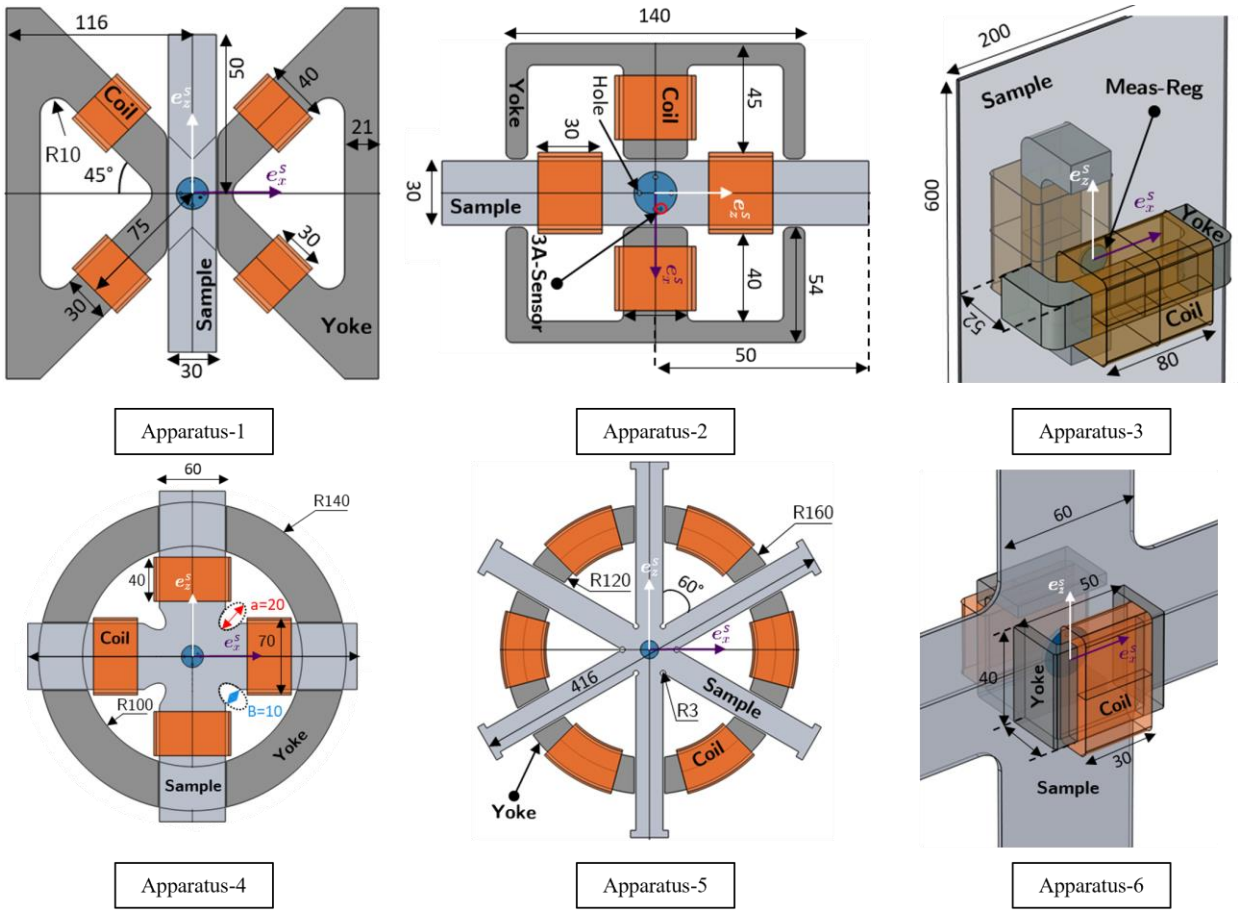

Fig.6. (Dimensions are in mm). The six studied apparatuses. The blue area is the ***B*** measurement region (i.e., a cylinder of height 2mm – equal to the sample thickness – and radius 10 mm) and position of the 3A-sensor (R_H origin: $x = 6.5$ mm, y $=$ 2.5 mm and $z = 2.5$ mm) of the 3A-sensor are the same for all apparatuses. The holes of 1 mm radius are 15 mm apart (see apparatus-2). The first three apparatuses allow the application of only uniaxial stress, and the other three the application of both uniaxial and biaxial in-plane stress. The origin of sample reference frame R_s coincides with the center of the ***B*** measurement region. R_s and R_B (the reference frame attached to the B-sensor) are chosen to coincide.

The reasons for the choice of these apparatuses are as follows: apparatus-1 has all coils on the same material (*i.e.*, the yokes) in contrast to apparatus-2, where two coils are on the sample, and the other two are on the yokes. Apparatys-3 gives freedom on the yokes orientations and allows to have them manually rotated (like the one in [36]). The sample shape in apparatus-4 was inspired by one of the samples in [39]. Apparatus-5 is very close to the one in [44], and apparatus-6 can be considered as the biaxial version of apparatus-3. All samples have a center of symmetry, which coincides with the origin of the sample reference frame R_s. In all apparatuses, the ***B*** measurement region (a cylinder of height 2 mm – equal to the sample thickness – and radius 10 mm) and the position of the 3A-sensor

(R_H origin: $x = 6.5$ mm, y $= 2.5$ mm and $z = 2.5$ mm, coordinates taken with respect to R_s) are the same. Like in the previous section R_s and R_B (the reference frame attached to the B-sensor) are chosen to coincide. Other studies wherein the 3A-sensor position was different (R_H origin: $x = 0$ mm, y $=$ 2.5 mm and $z = 0$ mm) were also carried out. Though their results may differ from the ones presented here, the drawn conclusions remain the same.

1. Isotropic materials

The $B(H)$ curve is the same throughout the present subsection (dot markers in Fig.7(a)). Results for the six apparatuses (numbered 1 through 6) are given in the appendix. For each apparatus, alternating (Alt) and rotating (Rot) field loadings are studied, and 26 measurements are presented. These are summarized in Table III.

TABLE III

MEASUREMENTS CARRIED OUT FOR EACH APPARATUS. THE FIRST COLUMN GIVES THE TYPE OF MEASUREMENT (***H*** DIRECTION AND IN-PLANE ***H*** DIRECTION ARE GIVEN AS FUNCTIONS OF THE EXPERIMENT TIME). THE SECOND COLUMN GIVES THE LOCATION OF THE MEASUREMENT, AND THE FOURTH, THE NATURE OF THE APPROACH (ALTERNATING OR ROTATING).

Measurement	Location	Alt/Rot
$B(H)$	Point	Alt & Rot
	Surface	Alt & Rot
	Above surface ($H_{out} = 0$)	Alt & Rot
	Above surface ($H_{out} \neq 0$)	Alt & Rot
H direction	Surface	Alt & Rot
	Above surface	Alt & Rot
In-plane ***H*** direction	Surface	Alt & Rot
	Above surface	Alt & Rot
$H_z(H_x)$	Point	Rot
	Surface	Rot
	Above surface	Rot
$B_z(B_x)$	Surface	Rot
	Above surface	Rot

Each measurement is carried out with and without drilled holes in the ***B*** measurement region (holes radius equals 1 mm and are 15 mm apart). The results of the two apparatuses that fulfill the BHmC the most (*i.e.*, 3 and 6) are given in Fig.7. Fig.7(a) and (b) correspond to the alternating approach, those of the rotating appraoch are in Fig.7(c-e). Dot markers in Fig.7(a) give the real $B(H)$ curve, and solid (resp dashed) lines give the results without (resp with) holes. Measurements at the sample surface (assuming the out-of-plane field components B_y&H_y null) are in black, those above the surface using 3A-sensor (not assuming $H_y = 0$) are in red, and those assuming $H_y = 0$ are in blue. The measurement at the surface coincides with the real material behavior (this is true for all apparatuses), which implies that both uniformity and direction criteria are respected. The discrepancies emerging when ***H*** is no longer measured at the surface (3A and 2A) are the result of an ill-respected correspondence criterion (for 3A and 2A) and direction criterion (for 2A).

For all results, the presence of holes (represented by simply the absence of matter in the simulation) degrades the accuracy. It is worth emphasizing that in practice drilling a hole does not simply mean taking some matter out but also modifying stress distribution and material properties in its vicinity. Results in the appendix show that the out-of-plane component on the surface is null for all apparatuses; however, it can become large ($100H_{out}/H \approx$60%) at 1 mm from the surface for apparatuses 1 and 2. This shows that the assumption that, in 2D systems, the fields are mostly in-plane near the surface is not always valid. Fig.7(b) gives the in-plane field direction for the alternating loading conditions. Though currents in each direction are imposed (*e.g.*, for apparatus-6: $I_{ex}(t) = 2I_0 \sin(0.02t\pi) = 2I_{ez}(t)$ and for apparatus-3, $I_{ex}(t) = 0$ and $I_{ez}(t) = 2I_0 \sin(0.02t\pi)$), the field still changes direction throughout the experiment time. An auxiliary simulation, wherein $B(H)$ is linear, showed that this effect is due to the nonlinearity. In essence, since the material does not get magnetized uniformly, some parts will have higher permeability; as a result, they attract the field from the parts with lower permeability, thereby changing the field direction. Fig.7(b) shows that the change is more pronounced for apparatus-6 than 3. This is because yokes were mirror images of each other for apparatus-3 and at a right angle for 6. Fig.7(c-d) gives the results for the rotating approach. The rotating magnetic field is obtained by imposing sinusoidal currents with 90-degree phases (three-phase currents for apparatus-5 in the appendix). Apparatus-3 was chosen to compare results at midfield magnitude (solid lines in Fig.7(c-e)) and close to saturation (dashed lines and diamond markers in Fig.7(d-e)). Results in Fig.7(c) show that measurements at the surface without holes (solid black lines) are the most accurate—those above the surface yield loops (more pronounced for apparatus-6). The loops stem from the fact that the magnetic field at the surface (colinear with ***B***) is non-colinear with that above the surface.

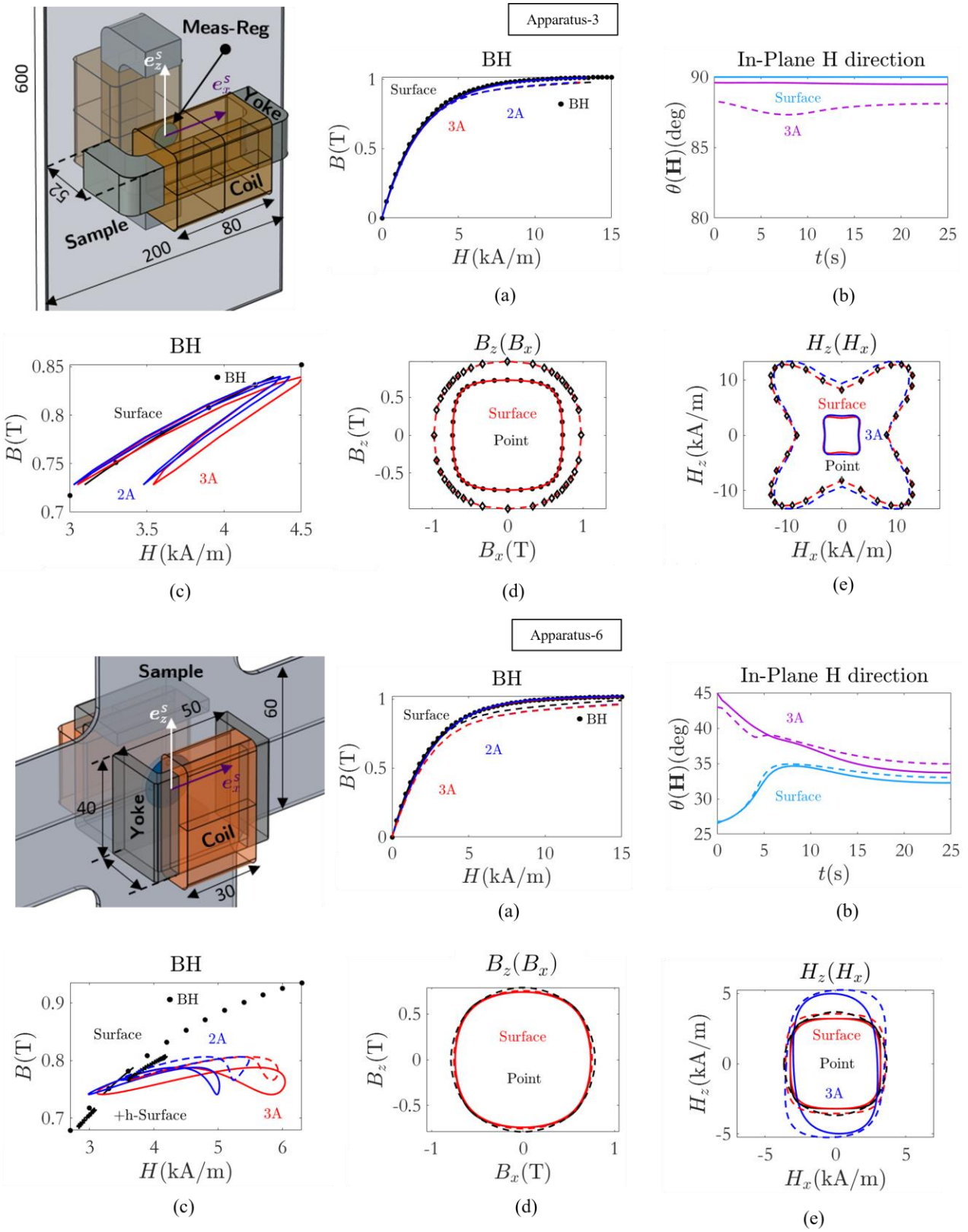

Fig.7. (a): Alternating results (seven curves): dot markers, give the real material behavior, solid (resp dashed) lines, give the measurement without (rep with) holes in the ***B*** measurement region. Measurements carried out at the surface are given in black, those using 3A-Sensor, in red, and those using 2A-Sensor in blue. (b): alternating results (four curves): the in-plane ***H*** field direction on the surface and at the 3A-Sensor location. (c-d-e): rotating results: for apparatus-3 they correspond to midfield magnitude (solid lines) and close to saturation (dashed and diamond markers), for apparatus-6, they correspond to the case without holes in the ***B*** measurement region (solid lines), and with holes (dashed lines).

Aside from the non-collinearity, such loops can result from misalignment between $\boldsymbol{B}$&$\boldsymbol{H}$ sensors (this was shown in a separate simulation). The fact that, once again, the 2A-Sensor results are closer to the real material behavior than those of the 3A-Sensor is merely due to two errors compensating each other. The first being the sensor is closer to the coils; as a result, $\boldsymbol{H}$ at the sensor location is larger than the one at the surface (giving rise to the measured $\boldsymbol{B}$). This correspondence error is compensated by the second error introduced by – only – the 2A-Sensor, since it measures the projection of the field (multiplying the norm by a cosine<1). Fig.7(d-e) gives $B_z(B_x)$ (resp $H_z(H_x)$). Note how imposing a circular current does not necessarily yield circular $\boldsymbol{H}$ or $\boldsymbol{B}$. Results of the rotating approach ($B_z(B_x)$ and $H_z(H_x)$) are functions of the excitation system, the sample material, and geometry. The fact that $H_z(H_x)$ is different from $B_z(B_x)$, is a result of the nonlinear behavior. This was shown in a complementary study using linear materials. While results for the six apparatuses may vary from each other, the conclusions remain the same: (1) the assumption that the fields are in the plane near the surface is not always valid (error $=[100H_{out}/H]$ can reach 80%, see apparatus-2 in the appendix). The direction criterion is thus respected by measuring all three vectorial components. (2) holes drilled in the sample reduce the fulfillment of the uniformity criterion, thereby degrading the measurement accuracy. (3) since $\boldsymbol{H}$ at 1 mm above the surface differs – both in magnitude and direction – from that at the surface (error$\approx 40\%$ for apparatus-6), the fulfillment of the correspondence criterion can be improved by moving the sensor closer to the surface and (4) when currents are imposed, the fields can change direction (resp magnitude) in alternating (resp rotating) approaches. The change of magnitude in the rotating loading was eliminated in a separate simulation wherein the yokes in apparatus-3 were set mirror images of each other and were rotated (instead of imposing circular current). They also can be eliminated if $\boldsymbol{B}$ or $\boldsymbol{H}$ are imposed.

2. Anisotropic materials

Apparatus-6 is chosen to assess the fulfillment of BHmC in the case of anisotropic materials. In the present case, anisotropy is not inherent to the material (like the one studied in Sec.II.A.2) but rather induced by applied mechanical stress. The analytical version of the multi-scale model (Daniel [46]) is used to model the effect of applied multiaxial stress on an isotropic material. Such a model gives the permeability in the direction of the applied magnetic field under applied multiaxial stress as:

$$\mu_i = 1 + \frac{A_i \sinh(\kappa H)}{A_i \cosh(\kappa H) + \sum_j A_{j\neq i}} \frac{M_s}{H} \qquad (8)$$

Where M_s is the saturation magnetization, $\kappa = \mu_0 A_s M_s$ (where $A_s = 3\chi_0/\mu_0 M_s$ and χ_0 the initial susceptibility of the anhysteretic curve under no applied stress), $A_i = \exp(\alpha\sigma_i), i \in \{x, y, z\}$, where $\alpha = (3/2)A_s\lambda_s$ (λ_s is the maximum magnetostriction strain). The numerical values of the parameters for the present case are: $M_s = 1.8\ 10^6$ A/m, $\kappa = 4 \times 10^{-3}$ m/A and $\alpha = 10^{-7}$ Pa^{-1}. Due to the high material permeability, the yokes permeability was set at 80 000 (instead of 10000 used thus far).

Fig.8 shows the results for alternating (first column) and rotating (second and third column) loadings. Dot markers correspond to the stress-free case, for which the material is isotropic. Continuous solid lines correspond to applied in-plane biaxial tensile stress ($\sigma_x = 10$ MPa and $\sigma_z = 20$ MPa). Dashed lines correspond to $\sigma_x = 10$ MPa and $\sigma_z = -20$ MPa. Black (resp red) color is used for measurement at a single point (resp surface), and blue color is used when the $\boldsymbol{H}$ field is measured using the 3A-Sensor above the surface. Measurements for the alternating approach are carried out when the yokes (mirror images of each other) are at a 30 deg angle from e_x^S (in the (e_x^S, e_z^S) plane. Other studies with the yokes at 0, 45, and 60 deg were also carried out; the conclusions, however, remain the same. For this loading, Fig.8(a) gives $B = f(H)$. Measurements at a single point and on the surface coincide, which implies that the uniformity criterion is respected. Measurements above the surface (green corresponds to when assuming $H_{out} = H_y = 0$) are significantly different from those at the surface. This stems from an ill-respected correspondence criterion. Grey curves in Fig.8(a) represent measurements carried out at the sample surface when holes are present. Note how the deviation between the stress-free and under-stress cases is the largest for such a case. The reason is that magnetic field and mechanical stress are concentrated around holes. As a result, the magneto-mechanical coupling amplifies the error due to non-uniformity. The effect of stress on the fulfillment of BHmC is more noticeable in Fig.8(b), wherein the in-plane directions ($\mathrm{atan}(H_z/H_x)$ and $\mathrm{atan}(B_z/B_x)$) as functions of the experiment time are presented. For the stress-free case, the fields remain at 30 deg throughout the experiment (*i.e.*, the direction set by the yokes), both at the surface and above the surface. When stress is applied, $\boldsymbol{B}$&$\boldsymbol{H}$ are no longer colinear and are not in the yokes direction. Their directions change over time and depend on stress. Fig.8(c) shows that with and without stress, $\boldsymbol{H}$ above the surface (at 1mm) is almost ($X(H_{out}) \approx 95\%$) normal to the surface.

The results for the rotating loading at $B \approx 0.7$ T (resp 1.7 T) are given in the second (resp third) column of Fig.8. Conclusions drawn from the alternating loading also apply here: (1) measurements at a single point and on the surface coincide (well-respected uniformity criterion), (2) those above the surface are significantly different (ill-respected correspondence criterion) and (3) the magnetic field at 1 mm from the surface is almost normal to the surface.

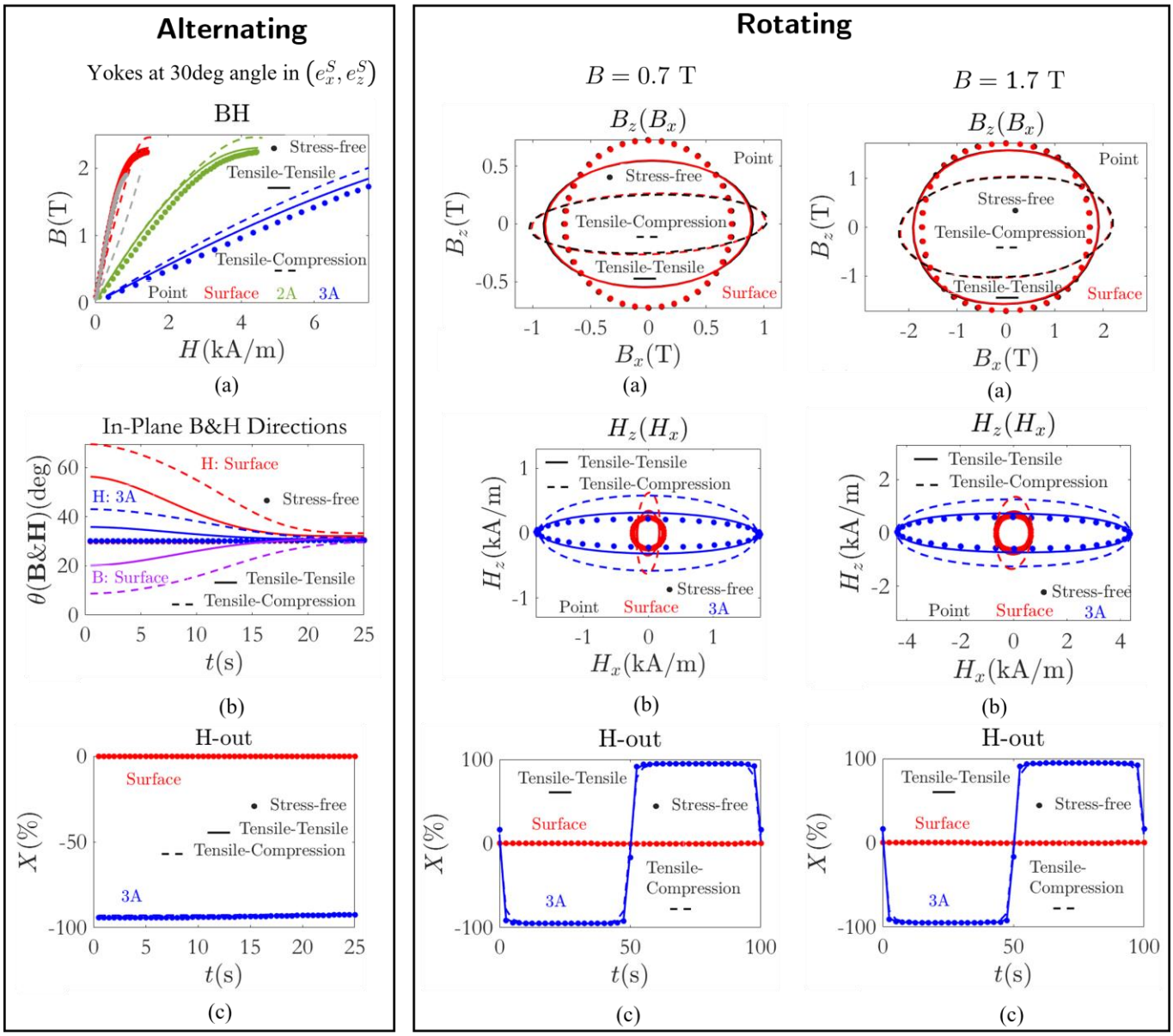

Fig.8. (Results for apparatus-6). Dot markers correspond to the stress-free case. Continuous solid (resp dashed) lines correspond to $\{\sigma_x = 10$ MPa and $\sigma_z = 20$ MPa$\}$ (resp $\{\sigma_x = 10$ MPa and $\sigma_z = -20$ MPa$\}$). Black (resp red) color is used for measurements at a single point (resp surface), and blue color is used when the $\boldsymbol{H}$ field is measured using the 3A-sensor above the surface. Alternating: In (a), green is used for when H_{out} is assumed null and the grey is used for when holes are present inn $\boldsymbol{B}$ measurement region.

IV. Conclusion

The present work dealt with the question of the magnetic characterization of magnetic materials. It puts forth three criteria that form a condition that is both necessary and sufficient for reliable measurements. These criteria are derived from the underlying assumptions made in every magnetic characterization experiment: (1) the material magnetic properties are assumed homogeneous in the measurement region (uniformity criterion). (2) the measured magnetic field $\boldsymbol{H}$ is equal to the one giving rise to the measured magnetic induction $\boldsymbol{B}$ (correspondence criterion). (3) $\boldsymbol{B}$&$\boldsymbol{H}$ directions are known throughout the experiment time (direction criterion). The criteria are indicators of how much these assumptions are respected for a given apparatus. The necessity and sufficiency of the criteria were first shown. Simulations were then used to assess their fulfillment for various apparatuses. Both alternating and rotating approaches were considered for linear and nonlinear behaviors, using isotropic and anisotropic materials in both 1D and 2D excitation and measurement systems, with and without applied mechanical stress. The main conclusions of the present work are: (1) When all three criteria are well-respected, measurements yield the material behavior. (2) Apparatuses with ill-respected criteria can yield constitutive relations that are significantly (an order of magnitude) different from the real ones. (3) Errors from ill-respected criteria can add to or subtract from each other. (4) Uniformity criterion is always well-respected for isotropic materials exhibiting linear

behavior. For anisotropic and/or nonlinear behavior, its fulfillment depends on material properties. (5) Improving uniformity criterion fulfillment can be achieved by decreasing the measurement region size and lowering the excitation frequency to avoid through-thickness non-uniformity due to eddy currents. (6) Drilled holes (to wound B-coils) introduce geometric inhomogeneity, thereby hindering uniformity criterion fulfillment. (7) Correspondence criterion is always respected if $\boldsymbol{B}$&$\boldsymbol{H}$ measurement regions coincide (*e.g.*, $\boldsymbol{B}$&$\boldsymbol{H}$ measurements are carried out at the sample surface). (8) $\boldsymbol{H}$ at 1 mm from the surface can significantly differ – in both magnitude and direction – from the one at the surface. (9) Misorientations between $\boldsymbol{B}$&$\boldsymbol{H}$ sensors can be reduced using isotropic materials. (10) $\boldsymbol{B}$&$\boldsymbol{H}$ directions should be known throughout the experiment time (direction criterion). (11) The fulfillment of the criteria can vary greatly from material to material and apparatus to apparatus. (12) apparatuses for which the $\boldsymbol{B}$&$\boldsymbol{H}$ measurements regions are far apart or using the magnetic path length method can hardly fulfill the measurement criteria and, if possible, should be avoided. In summary, the conclusions presented herein point towards two recommendations that are independent of apparatus and material properties: (a) measurements should be carried out in 3D space (B_{out} can be measured using the continuity of the normal magnetic induction component boundary condition). (b) If possible, both $\boldsymbol{B}$&$\boldsymbol{H}$ should be measured at the surface (in this case, through-thickness uniformity is not required, which allows to increase the frequency). If not, $\boldsymbol{H}$ should be measured as close to the sample surface as possible. Finally, while simulations were carried out using anhysteretic behavior and only a few sensor types were considered (i.e., Hall sensor, H-coil and B-coil), the conclusions presented herein remain the same for hysteresis and other types of sensors. This is because the measurement criteria are time-independent and, therefore, also apply to hysteretic behavior. Furthermore, active areas of sensors can be represented by points, surfaces, or volumes, which were all considered in the present work. It was also shown that in most cases, the criteria are satisfactorily fulfilled by 1D excitation systems. 2D systems offer more refined information (the ability to allow rotating fields and multiaxial loading), but they are prone to more significant measurement errors. Finally, this work shows the utmost importance of simulating the experimental setups before measurements to support the design and after measurements to quantitatively identify the uncertainty sources.

APPENDIX

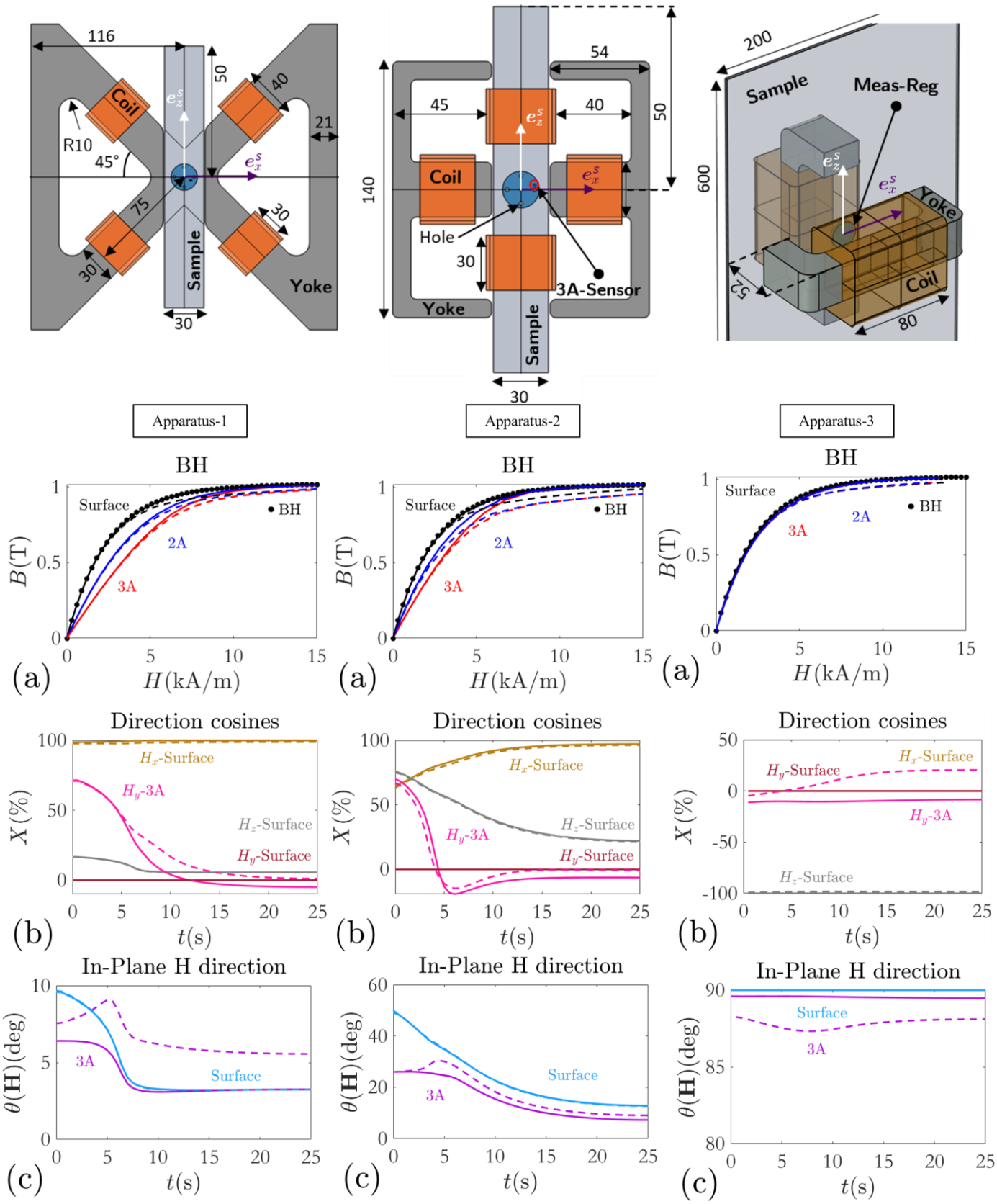

Fig.9. (Alternating results). All dimensions are in mm: apparatuses allowing for the application of only uniaxial stress. (a) contains seven curves: dot markers, give the real material behavior ($B(H)$), solid (resp dashed) lines, correspond to the case when there are no holes in the ***B*** measurement region (resp when there are). Measurements carried out at the surface (for both ***B***&***H***) are given in black, those using 3A-Sensor (resp 2A-Sensor) for ***H*** while ***B*** is measured at the surface, are in red (resp blue). (b) contains the direction cosines of ***H*** (*i.e.*, $X = 100H_i/H$) at the surface and the out-of-plane component (H_y) above the surface (at 1 mm, i.e., at the 3A-Sensor location) with (dashed lines) and without holes (solid lines). (c) contains 4 curves: the in-plane ***H***

field direction ($\theta = \mathrm{atan}(H_z/H_x)$) at the surface and at the 3A-sensor location, as a function of the experiment time with (dashed lines) and without holes (solid lines).

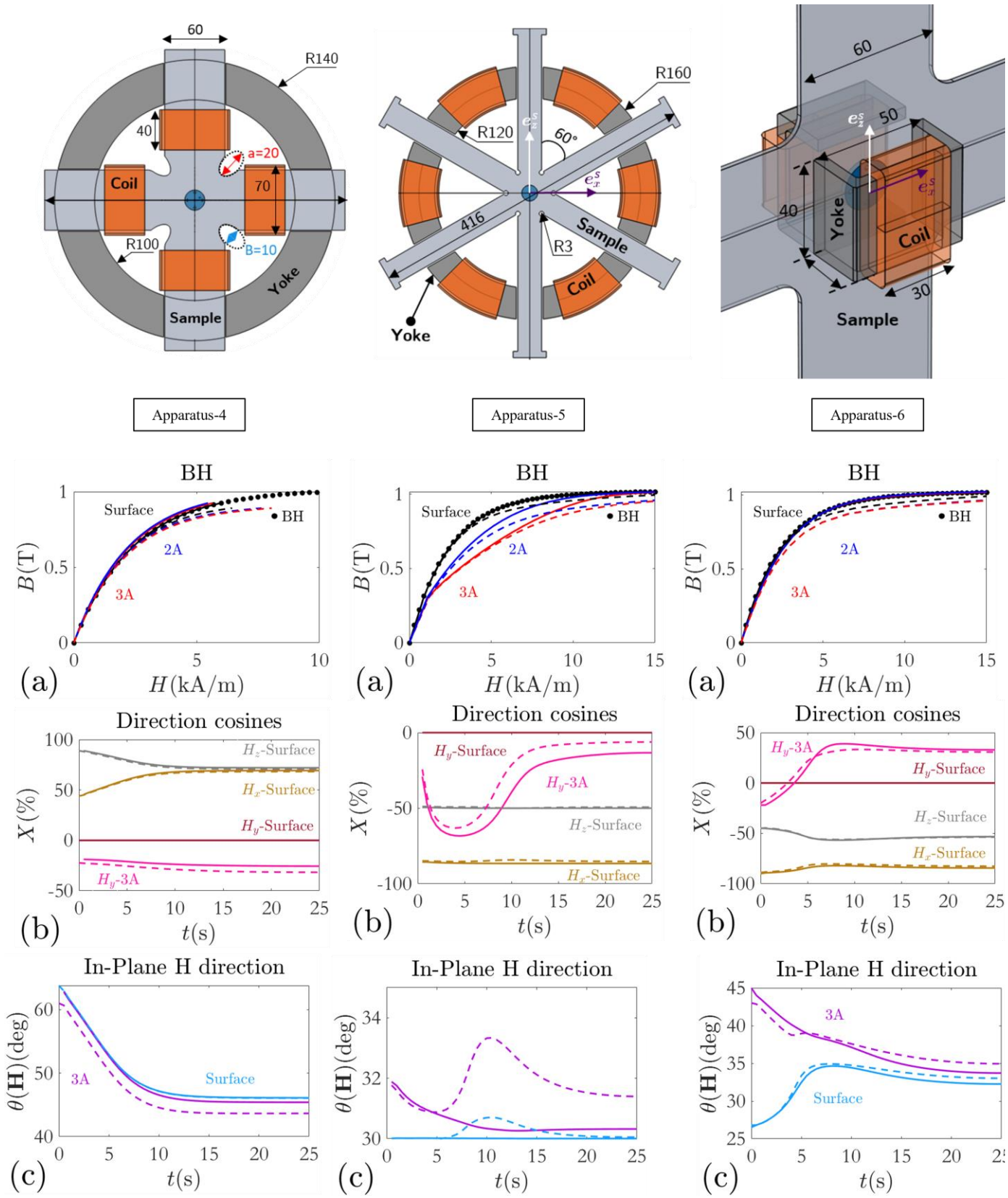

Fig.10. (Alternating results). All dimensions are in mm: Apparatuses allowing for the application of both uniaxial and biaxial stress. (a) contains seven curves: dot markers, give the real material behavior ($B(H)$), solid (resp dashed) lines, correspond to the case when there are no holes in the $\boldsymbol{B}$ measurement region (resp when there are). Measurements carried out at the surface (for both $\boldsymbol{B}$&$\boldsymbol{H}$) are given in black, those using 3A-Sensor (resp 2A-Sensor) for $\boldsymbol{H}$ while $\boldsymbol{B}$ is measured at the surface are in red (resp blue). (b) contains the direction cosines of $\boldsymbol{H}$ (*i.e.*, $X = 100H_i/H$) at the surface and the out-of-plane component (H_y) above the surface (at 1 mm, i.e., at the 3A-Sensor location) with (dashed lines) and without holes (solid lines). (c) contains four curves: the in-plane $\boldsymbol{H}$ field direction ($\theta = \mathrm{atan}(H_z/H_x)$) at the surface and at the 3A-sensor location, as a function of the experiment time with (dashed lines) and without holes (solid lines).

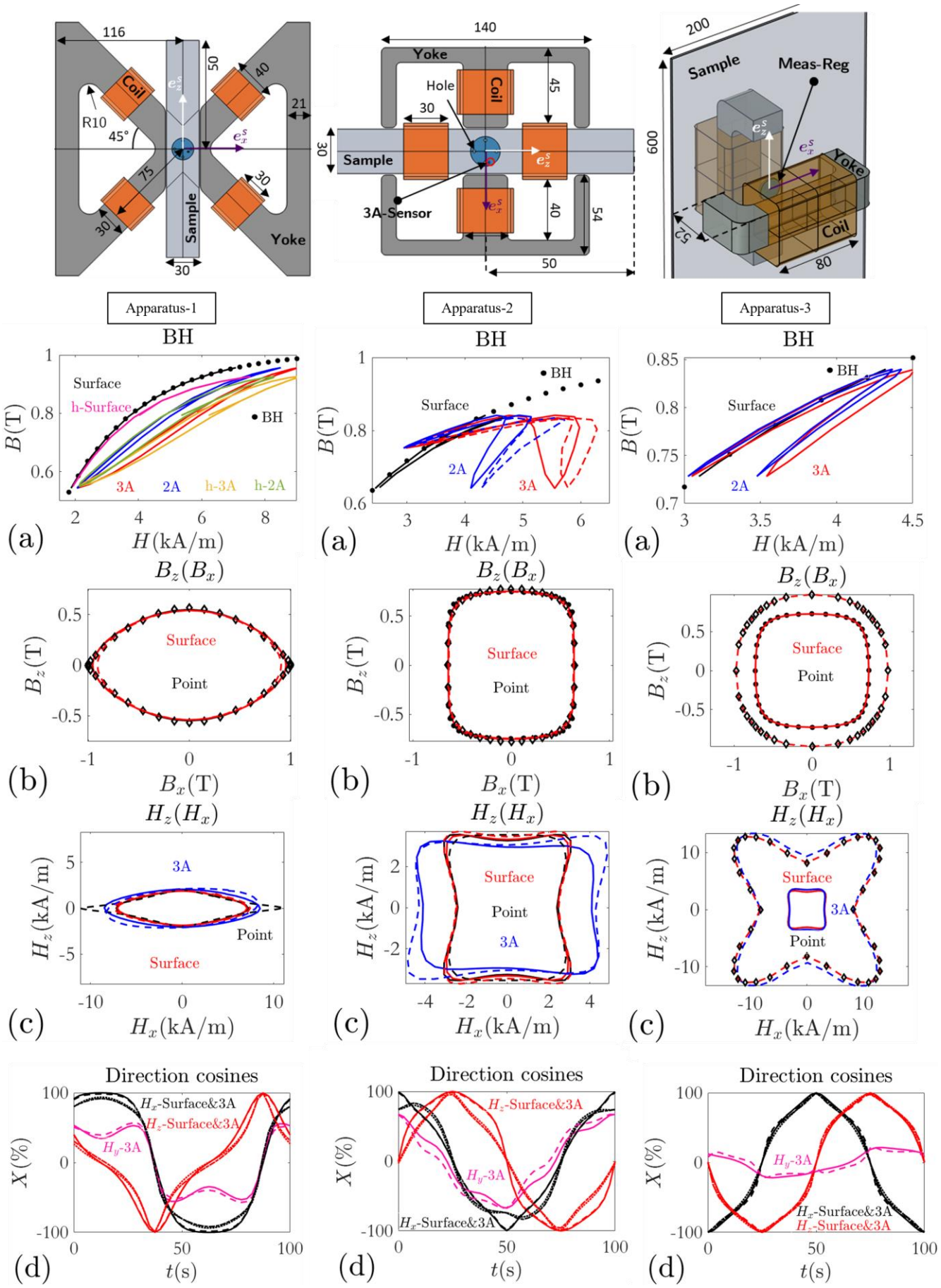

Fig.11. (Rotating results). All dimensions are in mm: apparatuses allowing for the application of only uniaxial stress. (a): dot markers, give the real material behavior ($B(H)$). For apparatus-1 (resp apparatus-2) the presence of holes is indicated by using "h" in the legend (resp dashed lines). For apparatus-3, measurements are carried out without holes. (b) for apparatus-1 and 2

dashed and diamond markers give measurements with holes; for apparatus-3, they give measurements close to saturation ($B \approx$ 1T). (c) $H_z(H_x)$ at a point in the material (black), at the surface (red) and at the 3A-Sensor location (blue). (d) contains ten curves: direction cosines ($X = 100H_i/H$) of the $\boldsymbol{H}$ field at the surface and at the 3A-Sensor location. Dashed (resp solid) lines represent for apparatus-1 and 2, the case with holes (resp without holes), and for apparatus-3 midfield magnitude (resp close to saturation).

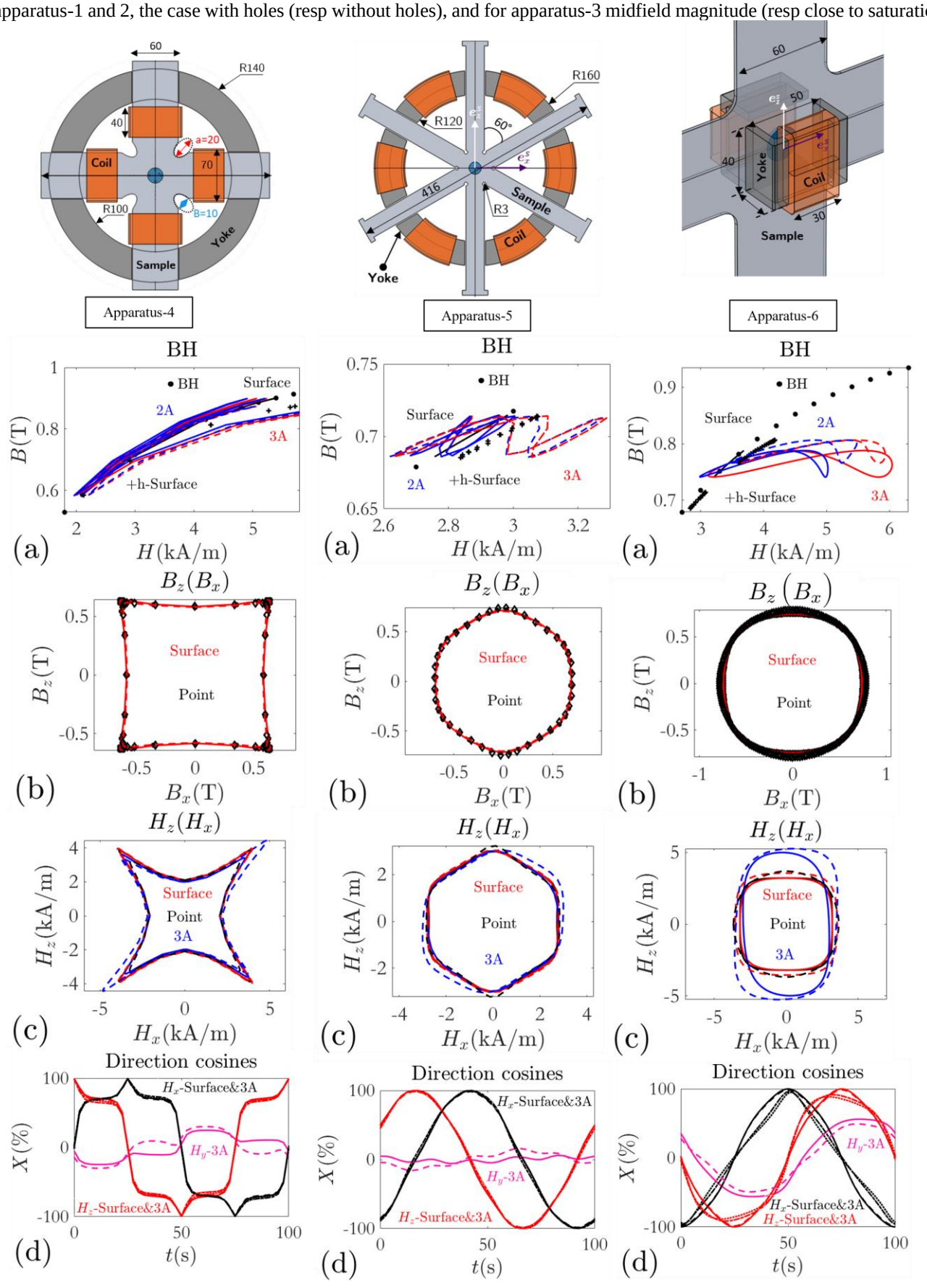

FIG.12. (Rotating results). All dimensions are in mm: apparatuses allowing for the application of both uniaxial and biaxial stress. (a): dot markers, give the real material behavior, solid (resp dashed and "+" markers) lines, give the measurements when there are no holes in the $\boldsymbol{B}$ measurement region (resp when there are). (b) $B_z(B_x)$ at a single point and on the surface for

when there are holes (dashed lines and diamond markers) and when there are not (solid lines). (c) $H_z(H_x)$ at a point in the material (black), at the surface (red), and at the 3A-Sensor location (blue) (d) contains ten curves: direction cosines ($X = 100H_i/H$) of the $\boldsymbol{H}$ field at the surface and at the 3A-Sensor location. Dashed (resp solid) lines represent for apparatus-1 and 2, the case with holes (resp without holes), and for apparatus-3 midfield magnitude (resp close to saturation).

REFERENCES

[1] R. M. Bozorth.: Ferromagnetism. Van Nostrand Company, New York, USA: 1951, pp. 595–712.

[2] B. D. Cullity, C. D. Graham.: Introduction to Magnetic Materials. Wiley, New Jersey, USA: 2011, pp. 241–273.

[3] DC Jiles, DL Atherton, "Theory of the magnetisation process in ferromagnets and its application to the magnetomechanical effect," *J. Phys D: App Phys*, 17, 1265 (1984), doi: 10.1088/0022-3727/17/6/023.

[4] DC Jiles, "Theory of the magnetomechanical effect," *J. Phys D: App Phys*, 28, 1537 (1995), doi : 10.1088/0022-3727/28/8/001.

[5] L. Daniel, M. Rekik, O. Hubert, "A multiscale model for magneto-elastic behaviour including hysteresis effects," *Arch Appl Mech*, 84(9):1307-1323 (2014), doi 10.1007/s00419-014-0863-9.

[6] L. Bernard, L. Daniel, "Effect of Stress on Magnetic Hysteresis Losses in Switched Reluctance Motor: Application to Stator and Rotor Shrink Fitting," *IEEE. T. Magn*, 51,9 (2015), doi: 10.1109/TMAG.2015.2435701.

[7] M. J. Sablik, H. Kwun, G. L. Burkhardt, and D. C. Jiles, "Model for the effect of tensile and compressive stress on ferromagnetic hysteresis," *J App Phys*, 61, 8 (1987), doi: 10.1063/1.338650.

[8] J. Sievert, "Recent advances in the one and two-dimensional magnetic measurement technique for electrical sheet steel," *IEEE T. MAG*, 26, 5, (1990), doi: 10.1109/20.104796.

[9] T. Nakata, N. Takahashi, Y. Kawase, M. Nakano, M. Miura and J.D. Sievert, "Numerical analysis and experimental study of the error of magnetic field strength measurements with single sheet testers,", *IEEE T. MAG* , 22, 5 (1986), doi: 10.1109/TMAG.1986.1064405.

[10] Y. Enokizono. T. Suzuki., J. Sievert and J. Xu, "Rotational power loss of silicon steel sheet," *IEEE T. Mag*, 26, 5, (1990), doi: 10.1109/20.104798.

[11] S. Zurek and T. Meydan, "Errors in the power loss measured in clockwise and anticlockwise rotational magnetization. Part 1: Mathematical study," *IEEE Proc.-Sci. Meas. Technol*.,153, 4, (2006), doi:10.1049/ip-smt:20050072.

[12] S. Zurek, T. Meydan.: Rotational power losses and vector loci under controlled high flux density. *IEEE T. Mag*, 42, 10, (2006), Doi: 10.1109/TMAG.2006.879907.

[13] N. Stranges, R.D. Findlay, "Measurement of Rotational Iron Losses in Electrical Sheet,". *IEEE T. Mag*, 36, 5 (2000), Doi: 10.1109/INTMAG.2000.871989.

[14] W. Brix, K.A. Hempel, and W. Schroeder, "Method for the measurement of rotational power loss and related properties in electrical steel sheets," *IEEE T. Mag*, 18, 6, (1982), DOI: 10.1109/TMAG.1982.1062088.

[15] H. G. Ramos and P. S. Girão, "A rotating field automated measurement system for the characterization of ferromagnetic materials,". *J Appl Phys* 69, 5103 (1991), doi: 10.1063/1.348137.

[16] K. Mori, S. Yanase, Y. Okazaki, and S. Hashi, "2-D Magnetic Rotational Loss of Electrical Steel at High Magnetic Flux Density,". *IEEE T Mag*, 41, 10 (2005), doi: 10.1109/TMAG.2005.854908.

[17] A. Ivanyi, J. Fuzi, and H. Pfutzner, "2D/3D Models for a Three Phase Fed Single Sheet Tester," *IEEE T MAG*, 34, 5 (1998), doi: 10.1109/20.717702.

[18] J. W. Wilson, N. Karimian, J. Liu, W. Yin, C. L. Davis, A.J. Peyton, "Measurement of the magnetic properties of P9 and T22 steel taken from service in power station," *J. Magn. Magn. Mater*. 360, 52-58 (2014), doi: 10.1016/j.jmmm.2014.01.057.

[19] S. Yue, A. J. Moses, P. I. Anderson, Ch. Harrison, Y. Li, Q. Yang, "Measurement and analysis of the non-symmetry of transverse magnetisation and resulting loss in grain-oriented steel using a modified RSST,". *J. Magn. Mater*, 561,169671 (2022), doi: 10.1016/j.jmmm.2022.169671.

[20] S. Hilary, N. Kouakeuo, A. Solignac, R. Sabariego, L. Morel, M. Raulet, et al, "Internal Characterization of Magnetic Cores, Comparison to Finite Element Simulations: A Route for Dimensioning and Condition Monitoring," *IEEE Trans. Instrum. Meas*., 71, 1-5 (2022), doi: 10.1109/TIM.2022.3194905.

[21] M. Enokizono, I. Tanabe, T. Kubota, "Localized distribution of two-dimensional magnetic properties and magnetic domain observation,". *J. Magn. Mater*, 196-197,338-340 (1999), doi: 10.1016/S0304-8853(98)00739-2.

[22] Y. Guo, L; Liu, X. Ba, H. Lu, G. Lei, W. Yin, J. Zhu, "Measurement and Modeling of Magnetic Materials under 3D Vectorial Magnetization for Electrical Machine Design and Analysis,". *Energies*, 16, 417 (2023), doi: 10.3390/en16010417.

[23] O. Hubert, L. Daniel, "Multiscale modeling of the magneto-mechanical behavior of grain-oriented silicon steels. *J Magn. Mater*, 320,7 (2008), doi: 10.1016/j.jmmm.2008.01.013.

[24] L. Daniel, O. Hubert, M. Rekik, "A simplified 3D constitutive law for magneto-mechanical behaviour," *IEEE T. Magn*., 51,3 (2015), doi: 10.1109/TMAG.2014.2361643.

[25] M. Domenjoud, E. Berthelot, N. Galopin, R. Corcolle, Y. Bernard, L. Daniel, "Characterization of Giant Magnetostrictive Materials under static stress : influence of loading boundary conditions," *Smart Mater. Struct.*, 28,9 (2019), doi: 10.1088/1361-665X/ab313b.

[26] L. G. da Silva, A. Abderahmane, M. Domenjoud, L.Bernard, L. Daniel, "An extension of the vector-play model to the case of magneto-elastic loadings,", *IEEE Access*, 10 (2022), doi: 10:126674-126686.

[27] H. Kwun, G. L. Burkhardt, "Effects of grain size, hardness, and stress on the magnetic hysteresis loops of ferromagnetic steels,". *J. Appl. Phys*. 61, 1576 (1987), doi: 10.1063/1.338093.

[28] P. Rasilo, D. Singh, U. Aydin, F. Martin, R. Kouhia, A. Belahcen, and A. Arkkio.: Modeling of hysteresis losses in ferromagnetic laminations under mechanical stress. *IEEE T. Magn*., 52, 3, (2016), doi: 10.1109/TMAG.2015.2468599.

[29] M. Domenjoud, L. Daniel, "Effects of plastic strain and reloading stress on the magneto-mechanical behavior of electrical steels: experiments and modeling," *Mech. Mater*., 176:104510 (2023), doi: 10.1016/j.mechmat.2022.104510.

[30] W. Huang, Z. Tao, P. Guo, B. Wang, L. Weng, "High-frequency magnetic energy loss based on J-A model for gallium iron alloy rod under variable stress conditions," *J. Magn. Magn. Mater* 563 (2022), doi: 10.1016/j.jmmm.2022.169970.

[31] J-H Yoo, J. B. Restorff, M. Wun-Fogle and A. B. Flatau, "Induced magnetic anisotropy in stress-annealed Galfenol laminated rods," *Smart Mater. Struct*. 18,104004 (2009), doi 10.1088/0964-1726/18/10/104004.

[32] A. Daem, P. Sergeant, L. Dupré, S. Chaudhuri, V. Bliznuk and L. Kestens, "Magnetic Properties of Silicon Steel after Plastic Deformation,". *Materials*, 13, 4361 (2020), doi: 10.3390/ma13194361.

[33] B. Toutsop, B. Ducharne, M. Lallart, L. Morel, P. Tsafack, "Characterization of Tensile Stress-Dependent Directional Magnetic Incremental Permeability in Iron-Cobalt Magnetic Sheet: Towards Internal Stress Estimation through Non-Destructive Testing,". *Sensors*, 22,16, (2022), doi: 10.3390/s22166296.

[34] I.T. Gürbüz, F. Martin, U. Aydin, A.B. Asaf Ali, M. Chamosa, P. Rasilo and A. Belahcen, "Experimental characterization of the effect of uniaxial stress on magnetization and iron losses of electrical steel sheets cut by punching process, " *J. Magn. Mater*, 549,168983 (2022), doi: 10.1016/j.jmmm.2021.168983.

[35] B. J. Mailhé, L. D. Bernard, L. Daniel, N. Sadowski, and N. J. Batistela.: Modified-SST for Uniaxial Characterization of Electrical Steel Sheets Under Controlled Induced Voltage and Constant Stress. *IEEE Trans. Instrum. Meas*., 69, 12, (2020), doi: 10.1109/TIM.2020.3006682.

[36] B. Yang, H. Li, and A. Zhang, “Influences of non-coaxial magnetic field on magneto-mechanical effect of ferromagnetic steel,”. *Int. J. Appl. Electromagn. Mech.* 1,1–8 (2018), doi: 10.3233/JAE-171138.

[37] . Y. Maeda, S. Urata, H. Nakai, Y. Takeuchi, K. Yun, S. Yanase, and Y. Okazak, “Development of the apparatus for measuring magnetic properties of electrical steel sheets in arbitrary directions under compressive stress normal to their surface,” *AIP ADVANCES* 7, 056664 (2017), doi: 10.1063/1.4977760.

[38] H. Helbling, A. Benabou, A. Van Gorp, M. El Youssef, A. Tounzi, W. Boughanmi and D. Laloy, “Effect on magnetic properties of inhomogeneous compressive stress in thickness direction of an electrical steel stack,” *J. Magn. Mater*, 500,166353 (2019), doi: 10.1016/j.jmmm.2019.166353

[39] M.V. Upadhyay, T. Panzner, S. Van Petegem, H. Van Swygenhoven, “Stresses and Strains in Cruciform Samples Deformed in Tension,” *Exp. Mech*. 57:905–920 (2017), doi 10.1007/s11340-017-0270-6.

[40] R. Langman, “Magnetic properties of mild steel under conditions of biaxial stress,”. *IEEE T MAG*, 26, 4 (1990), doi: 10.1109/20.54015

[41] M. J. Sablik, “Modeling the Effects of Biaxial Stress on Magnetic Properties of Steels with Application to Biaxial Stress, “. Nondestr. Test. Eval. 12,2 (2007), doi: 10.1080/10589759508952837

[42] M. Rekik, O. Hubert, L. Daniel, “Influence of a multiaxial stress on the reversible and irreversible magnetic behaviour of a 3%Si-Fe alloy, “. *Int. J. Appl. Electromagn. Mech*., IOS Press, 44 (3-4) (2014), doi: 10.3233/JAE-141793.

[43] Y. Kai, Y. Tsuchida, T. Todaka, M. Enokizono, “Development of system for vector magnetic property measurement under stress,” *J. Electr. Eng*. 61, 7 (2010).

[44] U. Aydin, F. Martin, P. Rasilo, A. Belahcen, A. Haavisto, D. Singh, L. Daniel, and A. Arkkio, “Rotational Single Sheet Tester for Multiaxial Magneto-Mechanical Effects in Steel Sheets,”. *IEEE T Mag*, 55, 3, (2019), doi: 10.1109/TMAG.2018.2889238.

[45] Y. Kai, M. Enokizono, Y. Kido, “Influence of shear stress on vector magnetic properties of non-oriented electrical steel sheets,” *Int. J. Appl. Electromagn. Mech*. 44 (2014), doi: 10.3233/JAE-141799.

[46] L. Daniel, “An Analytical Model for the Effect of Multiaxial Stress on the Magnetic Susceptibility of Ferromagnetic Materials,” I*EEE T Mag*, 49, 5, (2013), doi: 10.1109/TMAG.2013.2239264.

TIM-23-04058